

An Idealized Direct-Contact Biomass Pyrolysis Reactor Model

R.S. MILLER and J. BELLAN

Jet Propulsion Laboratory, California Institute of Technology, Pasadena, CA 91109-8099

(submitted November 1, 1996)

A numerical study is performed in order to assess the performance of biomass pyrolysis reactors which utilize direct particle-wall thermal conduction heating. An idealized reactor configuration consisting of a flat-plate turbulent boundary layer flow with particle convection along the heated wall and incorporating particle re-entrainment is considered. Particle pyrolysis is modeled using the complex pyrolysis kinetics and particle model of Miller and Bellan (1996b) with one dimensional (1D) slab geometry. An initial evaluation of the simplified particle geometry assumption is made through comparisons with full multi-dimensional particle simulations and reveals that the 1 D particle model results in conservative estimates for total pyrolysis conversion times and tar collection. The observed deviations are due predominantly to geometry effects while directional effects from thermal conductivity and permeability variations are relatively small. Simulations are conducted for the flat-plate reactor with particle injection rates as large as 30 kg/hr . The results indicate that pyrolysis evolution is effectively uncoupled from the boundary layer flow and is determined predominantly by the wall temperature. This, and other related results, suggest that direct-contact reactors can potentially result in greater tar production efficiencies than other types of non-contact and semi-contact reactors. Tar yields are maximized for small particle sizes and wall temperatures of approximately 850K , whereas ratios of tar output to feedstock input rates are independent of injection rate under the conditions of the study.

Key words: biomass, boundary layer, modeling, pyrolysis, tar, vortex reactor, wood

1 INTRODUCTION

The pyrolytic conversion of biomass materials into organic tars for hydrogen fuel production is the subject of increasing scientific consideration. Interest in these processes is due to both the 'clean' burn associated with hydrogen fuel and also to the relatively widespread availability of raw biomass materials such as wood chips from the forest industry. To insure that these processes are commercially viable, both experimental and theoretical investigations are employed to study various aspects of the conversion process including: pyrolysis kinetics, tar conversion to hydrogen, porous wood chip dynamics, moisture removal and reactor configuration. These research

initiatives ultimately aim at the design and optimization of commercially viable biomass conversion reactors.

Several reactor configurations are currently under consideration for the pyrolytic conversion of biomass to aromatic tars. The most widely addressed is the fluidized bed reactor (for a recent review of fluidized bed dynamics see Lim *et. al.* 1995). The majority of results in these areas are from experiments involving bench scale reactors and utilize relatively fine particle sizes for kinetic studies. For example, Scott and Piskorz (1982) designed a bench scale reactor operating at relatively low feed rates of approximately 15 g/hr using aspen-poplar sawdust with particle sizes $\sim 100\mu\text{m}$. Their findings indicate an optimal reactor temperature of $\approx 775\text{ K}$ for which tar yields approach 65% by mass. At higher reactor temperatures, the experiments indicate that the relative rates for tar decomposition reactions increase, thus resulting in a reduction of actual tar yields with increasing temperature. Scott *et. al.* (1988) performed further studies employing both the fluidized bed reactor and a bench scale transport reactor. Their results for both cottonwood and maple wood indicate a similar optimal reactor temperature range for tar harvest. In addition, it is observed that for particle sizes sufficiently small such that the particle heat up time is much less than the total conversion time, the reactor temperature is the only parameter determining the tar yield. Unfortunately, such particle sizes are much smaller than available wood chip stock ($\sim 100\mu\text{m}$), and expensive grinding processes are not currently economical for commercial scale reactors,

Additional reactor configurations which have received relatively less scrutiny are those in the category of 'direct-contact' reactors. In these reactors, the biomass particles are held in direct-contact with a heated solid surface, usually through centrifugal acceleration, such that the majority of heat transfer to the particles is through direct conduction from the wall. It is thought that higher heating rates associated with direct conduction heat transfer can reduce particle conversion times while simultaneously increasing both the overall tar yield and range of feedstock particle sizes. There exists considerable evidence from individual particle studies that high heating rates can produce these effects (see e.g. Miller and Bellan 1996a); however, studies in real reactors remain limited and further research is needed before design and optimization are possible. In particular, effects of particle size, particle-particle interactions and the potential for reactor scaling to commercial sizes are only poorly understood

at the present time.

Two primary direct-contact reactor configurations appear promising. The 'vortex reactor' is composed of a cylindrical steel reaction chamber with heated walls (Dicbold and Power 1988). An inlet pipe of high velocity superheated steam injects the particles along a tangential path at the top of the cylinder. Grooves cut along the interior walls aid in maintaining a tight helical path for the particle trajectories within the reactor and large centrifugal accelerations force the particles against the hot wall. A re-entrainment tube is necessary in order to re-introduce the partially pyrolyzed particles back into the reactor inlet as particle residence times are generally much smaller than conversion times. Both the gaseous tar and char dust escape the reactor via an outlet tube located at the bottom center of the cylinder. Conversion to hydrogen gas is performed outside the primary reactor chamber (e.g. Chornet *et.al.* 1994). A second direct-contact reactor configuration is the 'rotating cone reactor' which operates on similar principles (Wagenaar *et. al.* 1994). In this case, the reaction chamber consists of an upturned conical chamber with heated walls which is rotated at large rotational velocities. Biomass particles are injected from the bottom of the cone and centrifugal accelerations provide for the direct particle-wall contact necessary for high heating rates. Currently, published work for both reactor types is limited primarily to 'cold flow' results and many questions remain before actual commercial applications are viable. In particular, further research is needed to determine the efficiency of direct-contact pyrolysis, optimal reactor temperatures, effects of the turbulent gas flow field and corresponding boundary layer, and range of particle sizes which can be economically pyrolyzed.

The present research is aimed at addressing several of these unresolved issues for direct-contact pyrolysis reactors using a theoretical/numerical study. In order to simplify the analysis such that the effects of pertinent physical processes can be appropriately separated and identified, an idealized reactor configuration is investigated. The 'flat-plate reactor' configuration is explained in Section 2 along with a mathematical activation of several sub-models necessary for the overall reactor modeling. Section 3 outlines the numerical solution procedures and presents results relevant to each individual sub-model. The coupling procedure for the sub-models and final reactor simulation results are the subject of Section 4. Conclusion and further discussions are provided in Section

S. In particular, we provide scientific explanations for the commercial desirability of direct-contact reactors when compared to other types of reactors (e.g. Graham et. al., 1994).

2 FLAT-PLATE REACTOR AND SUB-MODEL FORMULATION

in order to gain insight into the physics of direct-contact reactors it is convenient to investigate a simplified configuration which captures the primary aspects of such reactors, while reducing the complexity of the mathematical modeling and numerical analysis. In the present work, a 'flat-plate' reactor geometry is chosen as illustrated in Fig. 1. The reactor consists of a heated plate held at constant temperature T_w and of finite length L . A lower temperature turbulent stream of superheated water vapor is introduced at the inflow boundary with constant velocity ($u_{1,inflow}$) and temperature ($T_{1,inflow}$). The biomass feedstock particles are injected at the tip of the plate and are assumed to remain in direct-contact with the wall, mimicking the effects of centrifugal acceleration. No-slip conditions at the surface of the heated wall result in the spatial development of a turbulent boundary layer within which the particles are quickly embedded as they convect downstream. Particles exiting the domain are re-introduced at the plate's tip until pyrolysis is complete.

The flat-plate reactor is able to capture the dominant physics governing direct-contact reactors: all biomass particles experience heating due to both direct wall contact and convection through the surrounding gaseous flow. Both particle-particle interactions and particle-flow interactions are therefore incorporated within the reactor model. The simplified geometry allows for a two dimensional (2D) modeling which greatly simplifies the numerical treatment of the governing equations. According to industrial practice, the flat-plate reactor is 'operated' in a steady-state mode with specified injection rates of various feedstocks and particle sizes. The steady-state nature of the flow greatly simplifies the analysis of results; tar distributions within the boundary layer and exit rates are easily computed.

Mathematical modeling of the flat-plate reactor is accomplished by deriving accurate sub-models for each of the primary physical processes within the reactor, and then coupling the sub-models through appropriate boundary

conditions and conservation relations. The present reactor configuration requires three primary sub-models: 1) a model for the pyrolysis of a single macroscopic porous biomass particle, 2) a model for a single particle's trajectory through the external flow field accounting for drag and friction forces, and 3) a model for the turbulent boundary layer flow field. Coupling among the sub-models is in the form of mass, momentum and energy exchange among the individual particles, the wall and the turbulent flow. The remainder of this section is devoted to the presentation of each of the sub-models along with a discussion of related assumptions.

2.1 Particle pyrolysis model

As will be discussed below, the particle height must be significantly smaller than the boundary layer thickness in order to satisfy the assumptions for the boundary layer gas flow. Assuming that the gas flow enters the reactor as fully turbulent pipe flow, the initial boundary layer thickness is approximately equal to one half the inflow pipe diameter and then grows as the downstream distance to the $4/5$ power (Burmeister 1983). For example, the inflow pipe diameter is 1.1 cm for the NREL reactor (Diebold and Power 1988) which places an upper limit on the particle height of approximately 5mm. The relatively small particle sizes as compared to the boundary layer thickness suggest that the particle quickly becomes embedded deep into the layer, within the 'laminar sub-layer' region. It is additionally assumed that a particle model incorporating quiescent flow adjacent to the particle will satisfy the constraints of the model; an *a posteriori* analysis of the results confirms the validity of the assumption, even for the case of relatively large particle Stokes numbers ~ 100 , as will be discussed below. The macro-particle pyrolysis model of Miller and Bellan (1996b) is therefore chosen as the particle sub-model since it embodies these assumptions. The kinetics scheme for the model is based on superimposed cellulose, hemicellulose and lignin reactions, and has been shown to compare favorably with experiments. Its primary advantage is that any biomass feedstock can be simulated through the knowledge of its initial mass composition with respect to these three primary components. Each of the virgin components undergoes an initial depolymerization reaction:



This is followed by two primary competing decompositions; an endothermic reaction to tar:



and an exothermic formation of char and gas:



Secondary tar decomposition is also exothermic and is modeled as a single step irreversible reaction:



All reactions are modeled with first order Arrhenius kinetics. The frequency factor-s and activation energies for each reaction, and the mass ratio X , are all dependent on the particular biomass component, whereas all heats of reaction and secondary tar decomposition parameters are independent of the source component. All values for activation energies and frequency constants are provided in Miller and Bellan (1996b).

The internal particle dynamics are governed by the following set of equations presented in general tensor form (summation over repeated, non-Greek indices). The apparent density (ρ) for solid phase species is governed by:

$$\frac{\partial \rho_{s,\xi}}{\partial t} = \dot{S}_{s,\xi}, \quad (5)$$

whereas the continuity equation for the gas phase includes a term for convection due to velocity field u_i :

$$\frac{\partial \rho_g}{\partial t} + \frac{\partial}{\partial x_j} (\rho_g u_j) = \dot{S}_g, \quad (6)$$

where the apparent densities are related to the true densities ($\hat{\rho}$) via the porosity ε (ratio of pore volume to total volume),

$$\rho_g = \varepsilon \hat{\rho}_g, \quad \rho_{s,\xi} = (1 - \varepsilon) \hat{\rho}_{s,\xi}, \quad \varepsilon = 1 - \sum_s \rho_{s,\xi} / \hat{\rho}_{s,\xi}, \quad (7)$$

The subscripts refer to the phase (s- solid, g- gaseous) and the species (ξ), the summation is over all solid phase species, and the source terms on the right hand side of the equations are defined by the appropriate Arrhenius

rates discussed above. Gaseous species mass fraction (Y), total specific internal energy ($e_t = e_s + e_g$) and the state equations are:

$$\frac{\partial \rho_g Y_\xi}{\partial t} + \frac{\partial}{\partial x_j} \left[\rho_g Y_\xi u_j - \rho_g D_{eff}^{(\xi)} \frac{\partial Y_\xi}{\partial x_j} \right] = \dot{S}_{g,\xi}, \quad (8)$$

$$\frac{\partial e_t}{\partial t} + \frac{\partial}{\partial x_j} \left[e_g u_j - \lambda_{ij}^{eff} \frac{\partial T}{\partial x_i} \right] = p\dot{\Omega} + \sum \dot{S}_\xi \Delta h_\xi, \quad (9)$$

and

$$p = \frac{\rho_g}{\varepsilon} \left(\sum^g Y_\xi / M_\xi \right) \bar{R}T, \quad (10)$$

where the velocity divergence is $\dot{\Omega}$, the heat of combustion is Δh , the molecular weight is M , the universal gas constant is \bar{R} , the pressure is p , the temperature is T , and the specific energies are related to the heat capacity at constant volume (C_v) for gases and the heat capacity (C) for solids:

$$e_g = \rho_g \left(\sum^g C_v^{(\xi)} \right) T, \quad e_s = \left(\sum^s \rho_{s,\xi} C^{(\xi)} \right) T \quad (11)$$

The effective (eff) species diffusivity is modeled based on porous media transport theory:

$$D_{eff}^{(\xi)} = \varepsilon D^{(\xi)}, \quad (12)$$

and the effective thermal conductivity includes radiation effects through the solid phase media and is modeled based on a volume average of solid and gas phase contributions:

$$\lambda_{ij}^{eff} = (1 - \varepsilon) \left\{ \frac{\sum^s \rho_\xi \lambda_{ij}^{(\xi)}}{\sum^s \rho_\xi} + \frac{\sigma d T^3}{\psi} \delta_{ij} \right\} + \varepsilon \sum^g Y_\xi \lambda_{ij}^{(\xi)}. \quad (13)$$

in the above formulation, σ is the Stefan-Boltzmann constant, d is a characteristic pore length scale, ψ is the emissivity, and δ_{ij} is the Kronecker delta function tensor,

Two momentum equations are considered in the present work for the purpose of comparisons. The first is the empirical Darcy's law which is valid only within the particle; it states that the velocity is proportional to the local pressure gradient and the permeability ($1/\mu$):

$$u_i = -\frac{1}{\mu_g} \lambda_{ij} \frac{\partial p}{\partial x_j}, \quad (14)$$

where μ_g is the gas viscosity. The second momentum equation is from Miller and Bellan (1996a) which is derived from first principles with relatively minimal modeling and is valid for both the particle interior and exterior regions:

$$\frac{\partial \rho_g u_i}{\partial t} + \epsilon \left[\frac{\partial}{\partial x_j} (\rho_g u_i u_j) \right] = - \frac{\partial p}{\partial x_i} + \frac{\partial \tau_{ij}}{\partial x_j}, \quad (15)$$

$$\mu_{eff} = \epsilon \sum^g Y_\xi \mu^{(\xi)}, \quad (16)$$

$$\tau_{ij} = 2\mu_{eff} \left[S_{ij} - \frac{1}{3} \frac{\partial u_i}{\partial x_i} \delta_{ij} \right], \quad S_{ij} = \frac{1}{2} \left(\frac{\partial u_i}{\partial x_j} + \frac{\partial u_j}{\partial x_i} \right). \quad (17)$$

Both forms of momentum equations are investigated in the following section for the purpose of comparing 1D and 2D Cartesian geometry simulation results. All property values are given in Miller and Bellan (1996b). Note that in the above set of equations both the thermal conductivity and the permeability are presented in full tensor format in order to account for spatial variations as addressed below.

Boundary conditions are defined based on the geometry under consideration and the particular choice of momentum equation as explained below. Particle shapes are assumed to be parallelepipeds based on elongated wood ‘splinters.’ These shapes have been observed in cold flow visualizations in the bench scale vortex reactor at the National Renewable Energy Laboratory (NREL) (e.g. Diebold and Power 1988). Throughout the present work only Cartesian geometries are considered for both 1D and 2D particle analyses. Boundary conditions on the wall side of the particle are independent of the momentum equation: the temperature at the solid surface is matched to the wall condition ($T = T_w$), the velocity is set to zero, and all other fluxes are nulled (zero first derivative). Darcy’s Law being valid only within the particle, the model domain extends only to the outer edge of the particle; thus, the thermal boundary condition in direction i is based on a modeled surface condition (see e.g. DiBlasi 1993):

$$-\lambda_{ij}^{eff} \frac{\partial T}{\partial x_j} = \sigma (T^4 - T_\infty^4) + h' (T - T_\infty), \quad (18)$$

which states that the heat flux entering the particle is due to both radiative and convective exchange with the far field temperature T_∞ . In the present work, the coefficient of convection is assumed to be constant with

$h' = -20W/K$. The pressure is assumed constant and equal to the far field condition. With the momentum equation derived from first principles (Miller and Bellan 1996a), the solution domain includes regions outside of the particle, thereby accounting for the effects of exothermic tar reactions within the mass boundary layer immediately adjacent to the particle. Then, boundary conditions are provided by directly matching temperature and pressure values to the flow conditions at the particle location ($T = T^*$, $p = p^*$, where the superscript indicates local flow values), while velocity conditions are calculated through mass conservation constraints, and mass fractions are assumed to have zero first derivatives at the boundary. The use of both momentum equations and the dimensionality of the simulations are considered in the following section,

2.2 Turbulent boundary layer model

The equations governing the boundary layer flow, which is assumed turbulent upon entering the reactor, are required to account for density variations due to the heated wall, mass exchange with particles, and exothermic tar reactions; in addition to accounting for the natural growth of turbulence in the near wall regions. The traditional approach for modeling such flows is to consider the 'long time averaged' Navier-Stokes equations of fluid motion with an appropriate turbulence model. Density variations are generally included through the use of Favre averages (mass weighted averaging). In general, such models contain a number of empirically defined constants obtained from experiments, therefore making their accuracy questionable for flows for which they are not calibrated. However, it is not always possible to find experiments by which to calibrate new constants; particularly in the area of multiphase flows. For example, flow measurements for a boundary layer, such as the one presently addressed, with a heated wall and multiphase flow are not available to the author's knowledge. There are related studies in which particles are uniformly distributed throughout the flow field at the inlet conditions (e.g. Hussainov *et. al.* 1995); a situation different from that of particles sliding along a heated wall. Earlier empirical studies of heat transfer in cone reactors have been conducted; however, insufficient data is provided to validate turbulence models (Szekely and Carr, 1966). Therefore, care must be taken in defining the conditions for which 'standard' turbulence models may be applied to the reactor boundary layer,

Several assumptions concerning the flat-plate reactor may be made in order to justify the use of a traditional single phase turbulence model for heated wall flow. If only particles with sizes smaller than the boundary layer thickness (well within the ‘laminar’ wall region) are considered, the flow can be assumed to ‘see’ the particles as a rough wall effect. Mass emissions of tar and gas from the particles are then assumed to act as a mild wall blowing condition. The two-equation $k - \omega$ model of turbulence (Wilcox 1988) offers a robust treatment of such flows including the effects of wall roughness and blowing. In this case, modeled equations for the turbulence energy k , and the specific dissipation rate ω are included along with the modeled Favre averaged Navier Stokes equations:

$$\frac{\partial \rho}{\partial t} + \frac{\partial}{\partial x_j} (\rho u_j) = 0, \quad (19)$$

$$\frac{\partial \rho u_i}{\partial t} + \frac{\partial}{\partial x_j} (\rho u_i u_j) = - \frac{\partial p}{\partial x_i} + \frac{\partial \hat{\tau}_{ji}}{\partial x_j}, \quad (20)$$

$$\frac{\partial \rho E}{\partial t} + \frac{\partial}{\partial x_j} (\rho u_j H) = \frac{\partial}{\partial x_j} \left[u_i \hat{\tau}_{ij} + (\mu_f + c_6 \mu_T) \frac{\partial k}{\partial x_j} + (\lambda + \frac{C_p \mu_T}{Pr_T}) \frac{\partial T}{\partial x_j} \right] + \sum \dot{S}_\xi \Delta h_\xi, \quad (21)$$

$$\frac{\partial \rho Y_\xi}{\partial t} + \frac{\partial}{\partial x_j} (\rho u_j Y_\xi) = \frac{\partial}{\partial x_j} \left[(\rho D + \frac{\mu_T}{Sc_T}) \frac{\partial Y_\xi}{\partial x_j} \right] + \dot{S}_\xi, \quad (22)$$

$$\frac{\partial \rho k}{\partial t} + \frac{\partial}{\partial x_j} (\rho u_j k) = \tau'_{ij} \frac{\partial u_i}{\partial x_j} - c_2 \rho \omega k + \frac{\partial}{\partial x_j} \left[(\mu_f + c_6 \mu_T) \frac{\partial k}{\partial x_j} \right], \quad (23)$$

$$\frac{\partial \rho \omega}{\partial t} + \frac{\partial}{\partial x_j} (\rho u_j \omega) = c_3 \frac{\omega}{k} \tau'_{ij} \frac{\partial u_i}{\partial x_j} - c_1 \rho \omega^2 + \frac{\partial}{\partial x_j} \left[(\mu_f + c_5 \mu_T) \frac{\partial \omega}{\partial x_j} \right], \quad (24)$$

where,

$$E = C_v T + k + u_i u_i / 2, \quad H = C_p T + k + u_i u_i / 2, \quad (25)$$

$$\hat{\tau}_{ij} = 2\mu \left[S_{ij} - \frac{1}{3} \frac{\partial u_i}{\partial x_i} \delta_{ij} \right] + \tau'_{ij}, \quad \tau'_{ij} = 2\mu_T \left[S_{ij} - \frac{1}{3} \frac{\partial u_i}{\partial x_i} \delta_{ij} \right] - \frac{2}{3} \rho k \delta_{ij}, \quad (26)$$

and

$$\mu_T = c_4 \frac{\rho k}{\omega}. \quad (27)$$

In the above equations, μ_T is the turbulence viscosity, C_p is the heat capacity at constant pressure, and the remaining variable notation is the same as defined above for the particle equations. All molecular property values

are assumed constant and equal to the corresponding values of pure superheated steam; more complicated analyses being unnecessary since $\mu_T \gg \mu$ except immediately at the wall surface where $\mu_T \rightarrow 0$. Values for the model constants are (Wilcox 1988):

$$c_1 = 3/40, \quad c_2 = 9/100, \quad c_3 = 5/9, \quad c_4 = 1, \quad c_5 = 1/2, \quad c_6 = 1/2 \quad (28)$$

and the turbulence Prandtl and Schmidt numbers are assumed constant with:

$$Pr_T = Sc_T = 0.9. \quad (29)$$

This is a two-equation turbulence model that has several advantages over the traditional $k - \epsilon$ turbulence models for the present flow. First, the equation for w can be integrated directly to the wall without the use of empirical wall functions; second, ω can take arbitrary, finite but non-zero values at the wall thus providing a natural means of modeling wall roughness and wall blowing effects through the use of boundary conditions (Wilcox 1988, Wilcox 1993).

In the above equations, three mass fraction equations are included for the steam, gas and tar species. The reaction source terms correspond to the tar decomposition reaction, and temperature and species fluctuations due to reaction terms are neglected. Neglect of these terms is justified for the present flow both because the exothermicity of the reactions is relatively mild, and because the residence time for the reactor ($t_r = L_{11}/u_{1, \text{in flow}}$) is significantly smaller than the Arrhenius reaction time scale for the conditions to be considered. Note that the above equation set does not contain direct couplings to the particles because these are included through boundary conditions at the wall. In addition, no separate notation is made for the boundary layer flow variables and the flow variables within the particle; the distinction is made clear by context.

The $k - w$ turbulence model equations describing the boundary layer flow is coupled to the heated wall through an appropriate choice of boundary conditions (see Fig. 1). Inflow conditions are based on a hyperbolic tangent function profile which allows for near constant values of flow variables away from the wall while smoothing the near wall region for matching to wall conditions. For example, in the present work the smoothing function for

temperature is $T = T_w + (T_{\text{inflow}} - T_w) \tanh(\kappa x_2/l_2)$ (κ is a weighting coefficient determining the degree of profile smoothing near the wall). Similar profiles are then applied to the remaining flow variables such as velocity, pressure, density, turbulence intensity and specific dissipation. The inflow mass fractions are also smoothed to match wall conditions while the free stream fraction for superheated steam is equal to unity. Outflow conditions are prescribed by setting the second derivative of all flow variables in the x_1 direction equal to zero which allows for linear behavior upon exiting the domain. Free stream conditions are obtained by prescribing null first derivatives of variables in the x_2 direction. At the wall, the streamwise velocity and the turbulence intensity are set null due to the no slip condition ($u_{1,w} = k_w = 0$), and the temperature is prescribed to be a constant, T_w . The pressure gradient is assumed null at the wall while density is determined from the equation of state. The specific dissipation at the wall is given by:

$$\omega_w = \frac{u_\tau^2}{\nu} S_R \quad (30)$$

where u_τ is the friction velocity, ν is the kinematic viscosity and the coefficient S_R determines the level of wall roughness or blowing (Wilcox 1988, Wilcox 1993). In the absence of particles, the cross flow velocity u_2 is zero at the wall, while null mass diffusion into the wall is satisfied through zero first derivatives for species mass fractions. Wall boundary conditions for the case of particulate flows are addressed in Section 4.

2.-? Particle trajectory model

The cold flow visualizations of Diebold and Power (1988) suggest that the majority of wood particles in the vortex reactor remain in flat contact with the wall, are parallelepiped in shape and in general convect with major axis (along the grain) parallel to the flow direction. This level of organization of the particulates is less likely in the cone reactor design in which there are no grooves cut into the chamber surface for particle guidance. In the present model, the particulates remain in contact with the wall. In addition, it is assumed that the particle's relative dimension in the transverse direction is constant with $l_3 = l_2$. Therefore, the particle dimensions are specified by the choice of the height l_2 and the aspect ratio $\Theta = l_1/l_2$. Lacking a complete resolution of the flow field around a real three dimensional wood particle, including the wake region, it is reasonable to assume

that the drag experienced by the particle can be modeled as that over an elongated (prolate) spheroid having the minor axis equal to l_2 and the same aspect ratio. Under these assumptions, the trajectory of a single particle is governed by both drag resulting from slip velocities with the exterior flow and by a friction force at the wall which impedes forward acceleration. The modeled equations for position and velocity (in the x_1 direction) are:

$$\frac{dx_p}{dt} = u_p, \quad (31)$$

$$\frac{du_p}{dt} = -f \left[\frac{18V_p\mu}{m_p l_2^2} \right] (u_1^* - u_p) - \alpha g, \quad (32)$$

where x_p and u_p are the instantaneous particle position and velocity, V_p and m_p are the particle volume and mass, α is the coefficient of sliding friction (assumed constant and equal to 0,1), g is the gravitational acceleration, and the modeled coefficient f is:

$$f = 1 + \frac{3\Delta Re_p}{16} + \frac{9\Delta^2 Re_p^2}{160} \ln(\Theta Re_p/2), \quad (33)$$

where,

$$Re_p = \frac{\rho^* |u_1^* - u_p| l_2}{\mu}, \quad (34)$$

and

$$\Delta = - \frac{8(\Theta^2 - 1)/6}{[(2\Theta^2 - 1)111 - ((3 + \sqrt{\Theta^2 - 1})/\sqrt{\Theta^2 - 1})] - \Theta}. \quad (35)$$

The bracketed term in [32] corresponds to Stokes drag over a sphere, whereas the factor f includes corrections for prolate spheroid aspect ratio at moderate particle Reynolds numbers (Clift *et.al.* 1978). The above equation set is Lagrangian and requires the specification of initial conditions for the particle position and velocity, in addition to the exterior flow field u_1^* .

3 SUB-MODEL SOLUTION AND EVALUATION

Before discussing the coupling of the individual sub-models, it is necessary to first analyze the behavior of each individual model and seek possible simplifications. This section is devoted to such analysis and includes discussions of the numerical solution procedure and range of parameters for each model, along with further useful

evaluations. In particular, although the particle model has been derived in general tensor coordinates, full multi-dimensional simulations are prohibitively intensive computationally. A comparison of 1D and 2D simulation results is made in this section in order to quantify the conditions under which the 1D approximation can be made. Simulation results from the single-phase boundary layer equations are also useful in determining the range of particle sizes which can be effectively treated through wall boundary conditions (*i.e.* when $l_2 \ll \delta_T$, where δ_T is the boundary layer thickness). The extent of individual particle response to external flow conditions is also investigated,

3.1 A multi-dimensional particle evaluation

In order to assess the effects of dimensional and directional effects for wood particles, the particle equations [5]-[14] are solved numerically on both 1D and 2D grids. Darcy's Law is used instead of the full momentum equation for several reasons. First, Darcy's Law is computationally less intensive than the full momentum equation [15] due to both the numerical treatment of the pressure solution, and also because the domain extends only to the edges of the particle, thus requiring fewer computational grid points than the full equation solution which extends to exterior regions. Second, the full momentum equation was developed for 1D solutions applied to relatively large permeability porous particles; as such, it does not explicitly include the effects of varying parallel and cross grain permeability. Miller and Bellan (1996) showed that the use of Darcy's Law can result in substantial over predictions of the surface temperature and pyrolysis rate. Therefore, it will be desirable to use the full equation for the final reactor calculations. However, for the present purposes of directional analysis, Darcy's Law is sufficient.

The numerical solution to the particle equations uses finite difference approximations to the governing equations. The solution procedure is essentially the same as applied in Miller and Bellan (1996) with the exception that Darcy's Law is combined with the continuity equation to provide an equation for pressure in order to filter acoustic waves while retaining density variations. The resulting Poisson type equation is:

$$\frac{\partial}{\partial x_j} \left(\frac{\rho_g}{\mu_g} \Gamma_{ji} \frac{\partial p}{\partial x_i} \right) = - \left(\dot{S}_g + \frac{\partial \rho_g}{\partial t} \right) \quad (36)$$

Directional effects for both the permeability and the thermal conductivity of the wood are considered; however, mixed directional property variations are not considered, *i.e.* $\lambda_{ij} = \lambda_{ji} = 0$, when $i \neq j$. Equation [36] is solved through a Jacobi iteration procedure at each numerical time step,

The geometry for the particle simulations is that of an elongated rectangular particle in flat contact with a hot constant temperature wall (see Fig. 1). Calculations are made with identical particle size in the x_2 direction, $l_2 = 5\text{mm}$, and 24 numerical grid points are used to partition the l_2 dimension, with equal grid spacing used for the parallel grain dimension ($l_1 = \Theta l_2$). The natural symmetry in the x_1 direction allows for the solution of only one half the entire domain. Values for the wood conductivity and permeability are also fixed in this direction as listed in Table 1 and correspond to approximate cross grain values for typical maple wood (SHRI 1979); all 1D simulations, results correspond to these cross grain property values. The kinetics scheme used for maple wood follows the method of Miller and Bellan 1996b by prescribing initial cellulose, hemicellulose and lignin content. The particle, wall and free stream temperatures are initially uniform at 400K and the pressure is $p = 100\text{kPa}$. During each simulation, the wall and free stream temperatures are both raised over a duration of 30s from 400K to their final values of $T_w = T_\infty = 900\text{K}$. The linear heating of the surface conditions is necessary for numerical resolution and does not affect the value of the results because the mass loss relative to the particle's initial mass is always $< 10\%$ at the final heatup time. All simulations discussed in this section are terminated when 90% of the virgin wood mass is consumed. For comparison, an entire 2D calculation utilizing 24×24 numerical grid points ($\Theta = 2$) requires approximately 6300s of central processor time on a Cray J916 supercomputer whereas the corresponding 1D simulation requires approximately 300s .

An example of direction property effects in a 2D particle simulation is illustrated in Fig. 2. The figure depicts instantaneous velocity vectors for the internal flow field for three different simulations of particles with aspect ratio $\Theta = 2$. The wall is located at the surface $x_2 = 0$ and the surface at $x_1 = 0$ is a plane of symmetry located at the actual center of the particle. In all cases, the vector snapshots are taken at a time corresponding to 40% reduction in the wood mass (virgin plus active). Particle initial conditions and properties are identical for all these

simulations including $\lambda_{11} = \lambda_{22}$, except the permeability which is varied in the parallel grain direction (λ_{11}). In general wood samples, the permeability in the parallel grain direction can exceed the cross grain permeability by several orders of magnitude (SERI 1979). The present results correspond to cases in which $\lambda_{11} / \lambda_{22} = 1, 10$, and 100, for parts (a), (b) and (c) of the figure, respectively. The vectors suggest that tar and gas produced by pyrolysis exit all surfaces of the particle nearly uniformly when there are no preferential permeability effects (Fig. 2a). However, when the permeability is increased parallel to the wood grain, the exiting gas flow is redirected nearly completely through the surfaces defined by $x_1 = \pm l_2$.

The preferential permeability effects illustrated in Fig. 2 can be quantified by examining the relative mass of tar collected from the particle as a function of time:

$$\beta = \frac{1}{m_{p,0}} \int_0^t \oint_A \rho_g Y_{tar} \vec{u} \cdot \vec{dA} dt, \quad (37)$$

where $m_{p,0}$ is the initial particle mass and the inner integral is over all surfaces. Tar collection for single isolated spherical biomass particles has been examined by Miller and Bellan 1996c who studied the effects of reactor temperature, tar quenching and parameter sensitivity. The mass of gas, or the combined masses could also be examined; however, it is the tar which is ultimately of interest for hydrogen production. Figure 3 shows the temporal evolution of β for each of the three 2D simulations in Fig. 2. Results from a 1D simulation are also included for comparison. The simulations suggest that there is virtually no deviation in the temporal mass loss due to preferential permeability effects. Only a very small increase in conversion time, with negligible change in final tar collection, is observed as the parallel grain permeability is increased by two orders of magnitude. This result is similar to a previous observation made by DiBlasi 1993 who found nearly no change in final char masses upon altering both the char and wood permeabilities in 1D simulations using Darcy's law. The 1D particle approximation is observed to slightly over predict conversion times and under predict all of the 2D tar collection results for all times. However, the final magnitude of β is only slightly lower than the maximum observed value from the 2D calculations.

In order to highlight the effects, and limitations, of the 1D approximation it is instructive to compare simulation

results for various values of the particle aspect ratio. Figure 4 depicts the tar collection as a function of time for both 1D and 2D simulations with particle aspect ratios of 1, 2 and 4. The simulation parameters are identical to those discussed above and both the permeability and the conductivity have constant uniform values in order to isolate geometric effects. The 1D case corresponds by definition to an infinite aspect ratio particle; however, the results show that the approximation becomes reasonable for realistic finite aspect ratios. Again, results for the 1D geometry produce conservative estimates for β at all times and all aspect ratios. The primary effect of particle geometry is observed in the total conversion time which decreases with decreasing aspect ratio. This effect is directly related to the surface area exposed to heating and pyrolysis relative to the total particle volume. On the other hand, the final values for β are much less influenced by the aspect ratio. In fact, the deviation in this value between the 1D approximation and a square particle is less than 5% of the initial particle mass. For $\Theta = 2$ this deviation is reduced to approximately 2.5%.

Biomass wood samples also have directional variations in thermal conductivity: a review of the literature shows that the conductivity is generally larger in the cross grain direction for both hard and soft woods. For example, measured ratios of $\lambda_{11}/\lambda_{22}$ for white pine, oak and balsa are approximately 0.75, 0.80 and 0.88, respectively (SERI 1979). These ratios are dramatically smaller in magnitude than those observed for permeability. The effects of these deviations are illustrated in Fig. 5 which shows β as a function of time for both the 1D and 2D simulations with three conductivity ratios. The aspect ratio is fixed at $\Theta = 2$ and $\lambda_{11}/\lambda_{22} = 1$ in all cases in order to isolate conductivity effects. As with the permeability, only relatively small effects of conductivity are observed for either the conversion time or the final tar mass. The 1D approximation again results in conservative estimates for tar production with time; however, the final tar conversion is well predicted. Further simulations were conducted with conductivity ratios as large as 10 (not shown) which resulted in very large deviations from the behavior exhibited in Fig. 5. Although such ratios are unrealistically large, they explain the permeability and aspect ratio behavior discussed when examining Figs. 3 and 4. Both conductivity and aspect ratio affect pyrolysis in a direct manner, *i.e.* the particle heating rate is a direct function of the ability to heat large portions of the wood

to pyrolysis temperatures. The majority of heat transfer into the particle occurs through conduction. As such, the conductivity plays a strong role in pyrolysis (even though realistic directional variations are relatively small as shown in Fig.5). The particle's aspect ratio also plays a strong role by dictating the surface to volume ratio of the particle which is exposed to heating. However, permeability primarily determines the path of the pyrolysis gaseous products upon being formed, resulting in only minor and secondary effects on the pyrolysis evolution even when large directional variations are present.

The above results suggest that the 1D particle geometry represents a valid approximation to the more complex multi-dimensional pyrolysis behavior for relatively large aspect ratio particles; in particular it produces conservative estimates of both tar collection and conversion time. The validity is not significantly affected by directional variations in the permeability, or for realistic values of the thermal conductivity. The approximation can also be considered justified for small aspect ratios ($\Theta \geq 1$) when only the final product yields are of interest. When the time evolution of pyrolysis products is needed, the 1D approximation results in over predictions of the conversion time. However, as will be discussed below, the deviations in total conversion time become negligible in the context of the flat-plate reactor discussed here, and the 1D approximation will, therefore be considered hereinafter. Furthermore, all simulations discussed hereinafter utilize the full momentum equation [15] in order to resolve the thermal and mass boundary layers adjacent to the particle surface, and the computational domain is extended to include the range $0 \leq x_2 \leq 1.5l_2$ for all simulations using a 32 grid point discretization. The value $1.5l_2$ is somewhat arbitrary; however, it is sufficiently large to resolve the region adjacent to the particle, while being small enough to allow for accurate sampling when the temperature and pressure boundary conditions are later matched to the boundary layer flow conditions. All further simulations are continued until 99% decomposition of the virgin wood is completed and with a thermal boundary condition heatup time equal to one second per millimeter thickness l_2 . Test cases comparing the results from single isolated 1D particle simulations with identical conditions using the two momentum equations reveal nearly identical evolutions (not shown).

“To conclude the discussions of isolated particle simulations, it is useful to analyze the efficiency of direct-

contact particle pyrolysis. This is accomplished by performing two 1 D simulations under the conditions previously discussed, *i.e.* $L_z = 5mm$, $T_w = 900K$, $T^* = 900K$, where T^* now corresponds to the local exterior flow temperature condition at $x_2 = 1.512$. In the first simulation, heating is only performed at the wall while the thermal flux is null in the free stream. The opposite conditions are employed for the second simulation; in this case heating is exclusively from the free stream and the wall is insulating. Both the tar collection and mass averaged particle temperature,

$$\langle T \rangle = \frac{\int_0^{l_2} \rho_s' T' \cdot dx_2}{\int_0^{l_2} \rho_s' \cdot dx_2}, \quad (38)$$

evolutions are presented in Fig.6. The superscript $'$ in the above equation denotes that solid phase char is excluded (Miller and Bellan 1996a, Miller and Bellan 1996b, Miller and Bellan 1996c). Clearly, the direct-contact wall heating provides a dramatically improved pyrolysis and heating rates as compared to the flow heating case. The total conversion time is decreased by approximately 65% by direct-contact conduction heat transfer. For free stream heating, although thermal transfer occurs both through convection and conduction, the thermal conductivity of the gases is nearly an order of magnitude smaller than for the solid phases. Mass averaged heating rates are observed to be as large as $\sim 10K/s$ for the wall heating case and can exceed the calculated values by small percentages for realistic multi-dimensional particles. Furthermore, larger heat transfer rates result in higher effective pyrolysis temperatures which yield significantly larger final tar collection values from direct conduction pyrolysis. These results suggest that direct-contact reactors offer a significant potential for improvement in pyrolysis yields for hydrogen production when compared to non-contact and partial contact (fluidized bed) reactors.

3.2 Turbulent boundary layer solution

The governing equations for the turbulent boundary layer flow are the $k-\omega$ equations [19]-[29] and their numerical solution is obtained using the second order time and space accurate McCormack scheme (e.g. Anderson *et al.* 1984) based on finite difference approximations. The physical domain has fixed dimensions $L_1 = 1.0m$, $L_2 = 0.4m$, and is discretized with 96 grid points in each direction, heavily compressed against the wall. In order to simplify the analysis of the results, only a single set of inflow conditions is considered and the solution

is determined entirely by the wall temperature and particle feed. Throughout the remainder of the paper, the boundary layer flow field is specified with the following inflow conditions: $u_{1,\text{inflow}} = 50\text{m/s}$, $T_{\text{inflow}} = 400\text{K}$, $p_{\text{inflow}} = 100\text{kPa}$ and $k_{\text{inflow}} = 18.75\text{ W/m}^2\text{/s}$. The wall roughness factor is $S_R = 0.5$ and the inflow ω value in the free stream is prescribed to be 10% of its wall value as given by [30]. As mentioned above, the inflow consists of pure superheated steam and thus all its properties are taken to be those of steam (Miller and Bellan 1996c). In each simulation, the entire flow field is initialized with the above set of inflow profiles for all x_1 and corresponding boundary conditions at the wall. The governing equations are then integrated in time until steady-state is reached. In general, this is achieved after a duration of five times the flow residence time t_r . An entire single phase calculation requires approximately one hour of central processor time on a Cray J916 supercomputer. An example illustration of the single phase boundary layer solution is provided in Fig.7 which shows both the numerical grid and also contours of the steady-state temperature field for the case where $T_w = 900\text{K}$. In the figure, the inflow is from the left hand side of the domain at which location the initial thermal boundary layer thickness is approximately 2cm . The thermal boundary layer then develops rapidly downstream and exits the domain with a thickness of more than 30cm . Contours of the streamwise velocity component are similar (not shown) to the temperature profiles; however, the velocity boundary layer thickness is somewhat less than the thermal layer thickness due to $Pr_T = 0.9$.

3.3 Particle trajectory and response to external flow field

The governing equations for an individual particle's trajectory [31]-[35] are Lagrangian and solved numerically through forward time differences. In order to analyze the characteristics of the equations as they relate to the final reactor flow, it is instructive to consider the trajectory of a single test particle through the single phase boundary layer flow field generated *a priori* (Fig.7). In the present example, a maple particle with $l_2 = 1\text{mm}$ and $\Theta = 2$ is chosen. Three additional inputs are required: the gas flow field u_1^* , the particle conversion time t_c which determines the duration of the simulation and the particle mass m_p as a function of time (the particle volume remains constant due to the residual char formation). The flow field u_1^* is extracted from the steady-state

boundary layer flow and corresponds to the streamwise velocity field located at the particle's centerline height $12/2$ (a linear interpolation is performed when the particle is between boundary layer grid points). The conversion time ($t_c = 31s$) is estimated from a 1-D particle simulation performed with wall temperature $T_w = 900K$ and estimated flow side temperature $T^* = 850K$, and the particle mass is modeled as a linear decay between the initial and final values overtime t_c . In the complete reactor problem, it is expected that these three simulations (particle, boundary layer and trajectory) would need to be performed simultaneously as they are inter-dependent; *i.e.* the particle development depends on u_1^* , T^* and p^* , which depends on mass emissions from the particle, which depend on the particle position x_p , etc... However, for the present purposes of illustration it is sufficient to consider only the isolated modeled trajectory equation.

The particle position and velocity are initialized with the boundary layer inflow conditions at $x_1 = 0$ and $u_p = u_1^*(x_1 = 0) \approx 2m/s$. If the particle exits the outflow region of the boundary layer domain it is re-entrained into the reactor by re-initializing these position and velocity values. The particle response to T^* and p^* (at $x_1 = x_p$ and $x_2 = -1.5l_2$) is the primary concern here because it is these two values which as a function of time define the free stream boundary conditions for individual particle simulations (ρ^* being determined by the state equation). These flow conditions are extracted from the steady-state boundary layer flow as a function of time at the instantaneous particle position and are illustrated graphically in Fig. 8 (of course, it is expected that in the coupled reactor simulations, the tar and gas ejections from each particle within the domain will alter the boundary layer flow field, thus coupling the processes). Each 'cycle' observed in the curves corresponds to one re-entrainment loop through the boundary layer. It is these time dependent functions which are needed as free stream boundary conditions for the individual particle in order to couple the single particle pyrolysis to the boundary layer flow. However, the numerical resolution of these functions is extremely difficult in the time frame of the particle conversion. This is because each time the particle exits the domain, a discontinuous drop in temperature (and rise in pressure) is experienced (Fig. 8). It is therefore desirable to be able to use the time average of these curves as particle boundary conditions; however, the oscillations in temperature and pressure are

relatively large and a justification is necessary before an average value can be used with confidence.

An analysis of the relative time scales is useful in predicting the particle response to boundary conditions. The majority of heat transfer to the particle from the free stream occurs through thermal diffusion (convective heat transfer is away from the particle due to the venting of pyrolysis gases). The ratio of the time scale for thermal diffusion through the gas to the particle residence time during one loop through the reactor is:

$$\frac{t_\lambda}{t_r} = \frac{\rho_g C_p l_2^2 / \lambda_g}{L_1 / u_{p,in}} \sim c (l_2)^3, \quad (39)$$

where c is a constant of proportionality and the injection velocity is assumed to be proportional to l_2 near the wall. In order to consider the particle pyrolysis evolution independent of temporal oscillations (and therefore well modeled using average boundary values), this ratio must be significantly larger than unity; *i.e.* the particle passes through the domain much faster than the thermal diffusion response time. Using properties for tar, $c \approx 1 \text{ mm}^{-3}$ suggesting that particles with sizes less than 1 mm are strongly influenced by thermal perturbations ($t_\lambda/t_r < 1$), while only particles larger than approximately 5 mm ($t_\lambda/t_r > 100$) can be justifiably assumed to respond only to average values for free stream boundary conditions.

To further assess the influence of boundary condition temporal oscillations on the particle, we calculate the particle response to a specified temporal disturbance into the free stream temperature boundary condition. This calculation is performed for a 1 mm particle ($t_\lambda/t_r \approx 1$) using a boundary temperature equal to $T^* = 850 + 25 \sin(\omega' t)$ (the amplitude of $\pm 25 \text{ K}$ is approximately the root mean square fluctuation calculated from the data in Fig. 8) and $T_w = 900 \text{ K}$. The temporal evolutions of tar collection produced from such simulations are presented in Fig. 9 for various values of the oscillation frequency. The value $\omega' t_c = 0$ corresponds to no temperature fluctuations, while $\omega' t_c = 30$ results in 30 periods and corresponds approximately to the number of re-entrainment loops observed in Fig. 8. As it is clearly observed, there is no effect on pyrolysis due to thermal disturbances. The reason for this behavior in spite of the low time scale ratio for the 1 mm particle size is provided through the graphical illustration of char apparent density profile evolution displayed in Fig. 10 for the $\omega' t_c = 0$ particle. The figure shows that even though there is a high temperature free stream boundary condition at $x_2 = 1.512$, the

direct conduction heat transfer from the $900K$ wall located at $x_2 = 0$ is significantly stronger. The char profiles reveal that the pyrolysis occurs almost entirely on the wall side which results in a pyrolysis wave moving outward, towards the free stream. Only a small fraction of the pyrolysis occurs on the free stream side as indicated by a small bulge in the char profiles near $x_2 = l_2$ for intermediate times. These results suggest that regardless of the time scale analysis, average values for free stream temperature and pressure boundary conditions result in no loss of information, as the pyrolysis is effectively decoupled from the free stream disturbances. In addition, these results provide further justification for the use of a particle pyrolysis model with quiescent adjacent flow (neglected cross flow), since effects from the flow side of the particle are minimal. This can be understood by considering that a co-flow can affect the tar collection [37] in one of two primary manners: 1) by changing the pyrolysis evolution and hence the mass of tar production, or 2) by affecting the ejection velocity at the particle surface (u_2 only, for 1 D simulations). The above discussions have already highlighted how the thermal pyrolysis evolution is controlled primarily by the wall conditions; hence co-flow effects on pyrolysis are negligible, in addition, there is a velocity boundary layer due to no slip conditions such that $u_1 \rightarrow 0$ at the particle surface. This indicates that the ejection velocity is determined primarily by the internal particle pyrolysis, and the co-flow can only dictate the direction of the pyrolysis gases upon exiting the particle, not the tar collection parameter, β . Therefore, a quiescent particle model can be used for the present flow with no significant loss of information,

4 REACTOR SIMULATION AND RESULTS

in this section, the individual sub-models discussed above are coupled in order to capture the behavior of the flat-plate reactor. The reactor is specified by prescribing both the mass feed rate of biomass particles:

$$\dot{m}_{feed} = nm_p l_3 u_{p,in}, \quad (40)$$

and the particle size distribution. In all calculations, the reactor transverse dimension is assumed to be $l_3 = 1.1 \text{ cm}$, equivalent to the inflow tube diameter for the vortex reactor at NREL (Dicbold and Power 1988), and the particle number density n is measured in particles per unit area along the wall. It is assumed that γ remains constant

throughout the reactor, which is equivalent to stating that as a group of particles convects downstream, any ‘clumping’ of particles as they are slowed by friction and/or drag is offset by an equal amount of transverse spreading; *i.e.* divergence free particle velocity field along the wall. For the present purposes, only monodisperse particle size distributions are considered. A list of the wood properties used in the calculation is given in Table 1 (remaining properties for char and the gaseous species can be found in Miller and Bellan 1996b). Implementation of the model for polydisperse distributions is addressed below.

4.1 Sub-model coupling procedure

The model coupling entails the numerical solution of each model in such a manner that the complete effects of all particles are captured along with their corresponding effects on the boundary layer flow field. For general time dependent flows, an accurate solution of the reactor equations would entail the numerical solution of separate particle equation sets for every individual particle. Consider a case with $\dot{m}_{feed} = 10 \text{ kg/hr}$, $L_z = 1 \text{ mm}$, $\Theta = 2$ and approximately 30 re-entrainment loops per particle. Equation [40] then predicts that there are more than 3×10^4 particles within the reactor at any given time; calculating their individual structure and trajectories is clearly beyond the capabilities of current supercomputers. However, the steady-state nature of the reactor yields a much simpler iterative coupling procedure as follows:

Step 1: Perform a numerical solution of the governing equations for the boundary layer flow ([19]-[29]) until a steady-state solution is reached. The boundary conditions at the wall for the first iteration are the ones described above, *i.e.* the single phase solution. Further iterations include the effects of particles through wall boundary conditions as described below in Step 4.

Step 2: Perform a single ID particle simulation ([5]-[17]) on domain $0 \leq x_2 \leq 1.512$ using the identical value of T_w as in the reactor boundary condition. Average values for T^* and p^* conditions at the free stream boundary are estimated for the first iteration, whereas later iterations use time average values over $[0, t_c]$; these values are obtained from calculations of the particle trajectory through the boundary layer flow field (see Step 3). Extract the mass $m_p(t)$ and mass flow rates $\dot{m}_{\xi, exit}(t)$ exiting the particle for tar, gas and steam as a function of time

(these represent the mass added to the boundary layer flow from a single particle). Due to the wall, all mass exits the particle at the free stream boundary and the surface exit area is $\Theta(l_2)^2$ (recall that $l_3 = l_2$).

Step 3: Perform a trajectory simulation for the single particle (I31]-[35]) using the particle mass $m_p(t)$ extracted from Step 2 and terminating at the final conversion time t_c . The flow field u_j^* is extracted from the steady-state boundary layer flow at location $x_1 = x_p$ and $x_2 = l_2/2$ using appropriate interpolation between grid points, as discussed previously. Extract the particle position $x_p(t)$ as a function of time.

Step 4: It is now possible to construct source terms due to the particle pyrolysis; these are used as boundary conditions of mass injection at the wall in the boundary layer flow calculations. From Steps 2 and 3, the mass additions of steam, tar and gas from a single particle are known as a function of time, in addition to the particle's position $x_p(t)$. Therefore, the total mass injection rate can be calculated to provide a u_2 velocity component at the wall resulting from each single particle at any time. To account for all particles that are within the boundary layer (x_{BL}), the sources are simply multiplied by the number density n :

$$\rho u_{2,w}(x = x_{BL}) = n \int_0^{t_c} \dot{m}_{exit} \delta(x_p - x_{BL}) dt, \quad (41)$$

where \dot{m}_{exit} is the total mass exit rate from each individual particle, δ is the delta function and the integral accounts for all re-entrainment loops through the reactor. To illustrate how this is implemented, first neglect re-entrainment and consider any arbitrary point along the reactor wall. Assume that the particles are injected in small discrete groups, or clusters, from the reactor tip. When, for small enough clusters, all particles within a group will show essentially the same pyrolysis evolution and average trajectory. Therefore, solving for one particle yields in fact the behavior of the entire cluster, and the total mass ejection rate equals the product of the ejection rate from a single particle multiplied by the total number of particles. For a steady, identical initial condition cluster injection, at each position along the wall there is always a cluster of particles having the exact state of pyrolysis and trajectory as the previous cluster. The validity of the argument relies on the steady-state nature of the reactor; otherwise different particles would be in different stages of pyrolysis when they reach a given position along the wall. Therefore, during steady-state reactor operation, the numerical solution of a single

particle's evolution defines the entire set of particles. Re-entrainment consists of further injections of partially pyrolyzed particles and its effects are additive.

in addition to the momentum wall inflow, wall boundary conditions are also required for each of the species' mass fractions. Simplistically, these could be calculated as the ratio of the contribution from each species to the total momentum:

$$Y'_\xi = \frac{\rho u_{2,w,\xi}}{\rho u_{2,w}} \quad (42)$$

with the individual species contribution calculated using [41] and by multiplying the integrand by Y_ξ . However, this neglects the diffusion flux (in addition to convection), which can be quite large in a boundary layer because of the relatively large turbulent diffusion ($\mu_T > \mu$) even in the vicinity of the wall. In order to correct for this effect, the mass fractions must be calculated including the diffusion velocity. Knowing that the correct amount of each species influx through the wall is given by [42], the corrected fractions (Y_ξ) are calculated through the equation:

$$\rho u_{2,w,\xi} = Y_\xi \rho u_{2,w} - (\rho D) + \left(\frac{\mu_T}{Sc_T} \right) \frac{\partial Y_\xi}{\partial x_2}, \quad (43)$$

where the first term on the right hand side is due to convection, and the second term (calculated at the wall) is influx due to diffusion (molecular plus turbulent). The species gradients are not known *a priori*, and therefore Y_ξ is calculated dynamically from the above equation during further boundary layer simulations.

Step 5: in order to couple the sub-models, an iterative procedure is applied by repeating Steps 1-4 until the solution converges. This is generally satisfied after only one or two iterations,

4.2 Reactor results

The size and number density of particles considered here are subject to restrictions resulting from the model assumptions. From the perspective of the turbulent gas flow, particles can be considered as wall effects only if $l_2 \ll \delta_T$, where δ_T is the boundary layer thickness; this places upper bounds on the particle size. Lower bounds on the particle size were initially suggested by the analysis of the relative thermal diffusion time scale

[39] in conjunction with the use of average values for T^* and p^* in the particle equation boundary conditions, although this restriction was removed after discovering that the majority of pyrolysis occurs at the wall (thus minimizing any effects of T^* and p^* perturbations). Nevertheless, restrictions do exist for the lower bound of particle size due to the assumption of direct-contact with the wall for all particles. In order for all particles to remain in direct-contact, the added contact area of all particles must be less than the reactor wall surface area, *i.e.* $A' = nN\Theta(l_2)^2 < I$, where N is the total number of re-entrainment loops per particle. Combining the relation for A' with [40] shows that $A' \sim N/l_2$ where all remaining parameters are fixed. Therefore, if N decreases with l_2 less than linearly (as results suggest), then one must ensure that l_2 is not too small; otherwise the particles cannot geometrically remain in contact with the wall. The lower bound for l_2 is, however, a function of other parameters such as the mass feed rate of biomass, and must be checked on a case by case basis. Note that using the same arguments, one finds an upper bound on the mass feed rate.

An example of a complete reactor simulation is illustrated by the steady-state tar fraction profiles shown in Fig. 11. The simulation is for a reactor with a wall temperature of $T_w = 900K$, and with a mass injection rate of $10kg/hr$ of maple wood feedstock with monodisperse size distribution: $l_2 = 1\text{ mm}$ and $\Theta = 2$. The number of loops through the reactor is large ($N \approx 30$) so that every position along the wall receives a nearly equal contribution from the pyrolysis during every loop. This results in a nearly constant value for momentum injection along the wall. However, the tar fraction depends on the mass fraction gradient at the wall, and thus has a dependence on location, as noted by the wall values in Fig. 11 b. The distributions of tar shown in the figure also indicate that maximum mass fractions are found immediately adjacent to the wall. This has implications for the placement of catalysts converting tar to hydrogen within the primary pyrolysis reactor.

In order to study the effects of several parameters relative to the optimization of tar extraction from the reactor, it is convenient to define a reactor efficiency variable (η) as the mass rate of tar exiting the reactor relative to the total biomass feed rate:

$$\eta = \frac{I_3}{\dot{m}_{feed}} \int_0^\infty \rho u_1 Y_{tar} dx_2, \quad (44)$$

where the integral is calculated at $x_1 = L_1$. This ratio is independent of the transverse reactor dimension (L_3) and provides a means of evaluating the reactor performance. Consider for example the effect of particle size. Reactor simulations are performed for three values of the particle size; $l_2 = 1\text{mm}, 2.5\text{mm}$ and 5mm , which span more than two orders of magnitude in particle mass. The remaining reactor and particle parameters are held constant at $T_w = 900\text{K}$, $\dot{m}_{feed} = 10\text{kg/hr}$ and $\Theta = 2$ and the efficiency factors calculated from the steady-state flow are plotted in Fig. 12. In agreement with previous studies of isolated spherical maple particles in hot quiescent steam of Miller and Bellan 1996c, the tar yields increase for decreasing particle sizes. However, the efficiency of the present reactor is nearly twice that obtained with the quiescent steam heating. This is a consequence of the direct-contact heating which maintains relatively large temperatures within the particle, despite the effects of endothermic reactions. Direct contact reactors therefore offer potential gains in pyrolysis efficiency relative to other forms of convective heating.

Figure 13 highlights the effects of the wall temperature T_w for two values of the particle size; both the feed rate and the particle aspect ratio are held constant at $\dot{m}_{feed} = 10\text{kg/hr}$ and $\Theta = 2$, respectively. The solid line labeled 'kinetic' corresponds to the absolute maximum limitation on the tar yield imposed by the kinetic parameters ($m_p \rightarrow 0$) provided that the tar decomposition is eliminated. In practice, the complete quenching of tar reactions is not possible and therefore, the kinetic curve represents a purely theoretical maximum tar yield. The most interesting aspect of the efficiency curves is the presence of a peak value in η for temperatures $T_w \approx 800\text{K}$. The presence of an optimal temperature for tar production was also found in past simulations of spherical maple particles in quiescent steam environments (Miller and Bellan 1996c). An optimal temperature of $\approx 775\text{K}$ has also been observed in the bench scale fluidized bed reactor experiments of Scott *et al.* 1988. The experiments were also for maple wood, but used much smaller particle sizes $\sim 100\mu\text{m}$. Their measured tar yields were approximately 80% at this temperature, in good agreement with the present kinetic approximation as would be expected for such small particles. For temperatures above optimal, the rate of tar-decomposition reactions increases, resulting in an overall decrease in tar yield.

Another interesting parameter is the mass feed rate of biomass particles into the reactor. The efficiency factor versus feed rate is presented in Fig. 14 for a reactor with $T_w = 900K$, $l_p = 2.5mm$ and $\Theta = 2$. The maximum value of $\dot{m}_{feed} = 30kg/hr$ violates the previous restriction for A' , *i.e.* there is more particle surface area than wall surface; however, it has been included in the study for the sake of comparison. Figure 14 clearly illustrates the degree of decoupling of the particle pyrolysis evolution from the actual reactor flow field. This was preliminarily discussed in connection with Fig. 10 in the context of particle decoupling from the temporal perturbations of T^* and p^* . However, the nearly complete independence of the reactor efficiency from the feed rate indicates that not even the average values of T^* and p^* strongly affect the pyrolysis. In fact, by merely having adequate guesses for their values, the boundary layer flow does not have to be solved, as the yield/efficiency of the reactor is essentially equal to that of a single particle. This would not be true for a reactor with slower quenching of pyrolysis tars, *i.e.* longer tar residence times (the tar entering the present flat-plate reactor is convected downstream and out of the domain much more rapidly than the characteristic time for tar decomposition reactions).

In light of the above observations and the assumptions of the model, it is not necessary to investigate the effects of other parameters such as the particle aspect ratio Θ , polydispersity or the reactor inflow pressure. Increases in Θ will linearly increase both the feed rate and the exit mass rate from individual particles. The decoupling observed in examining Fig. 14 indicates that the reactor efficiency will therefore remain unaltered by changes in the particle aspect ratio. Polydispersity can be incorporated into the model by simply discretizing the inflow particle size distribution into a finite number of size classes: (1) for each size class, a unique internal particle equation set is solved corresponding to the particle size represented by the particular class, and (2) results from each class are then superimposed. The decoupling discussed above indicates that the final results are simply the mass weighted average of the individual size class results. As for the pressure, the kinetics scheme used in the particle model was derived for near atmospheric pressures and does not include corrections for high pressure (Miller and Bellan 1996b).

5 CONCLUSIONS

A combination of theoretical and numerical analyses have been performed in order to address both design and optimization issues related to direct-contact biomass pyrolysis reactors. In order to simplify the problem, an idealized 'flat-plate' reactor was introduced. In this configuration, the reactor consists of a turbulent high speed gas flow of super heated steam flowing over a flat-plate at high temperature. Biomass particles are introduced at the plate tip and convect downstream, embedded within the spatially developing gas flow boundary layer, while remaining in direct-contact with the heated wall. Partially pyrolyzed particles exiting the domain are then re-introduced at the plate tip, thus simulating the effects of a reactor recirculation loop. The solution procedure involved the development of complex models for the primary sub-systems of the reactor which include the individual wood chip porous particles, the flat-plate turbulent boundary layer flow, and the trajectory equations for individual particles within the flow field. These sub-models were then coupled through appropriate choices of boundary conditions and conservation considerations.

The sub-models were chosen for their ability to capture the pertinent physics and were based on the requirements of each sub-system. The kinetics and porous particle model of Miller and Bellan (1996b) were chosen to simulate the individual particle pyrolysis. Both one dimensional (1D) and two dimensional (2D) Cartesian coordinate simulations were performed in order to assess the effects of geometry and spatial property variations for single particles. The results showed that the 1D model based on cross grain properties yields correct qualitative pyrolysis behavior while providing slightly conservative estimates for the quantitative particle conversion times. However, the total tar and gas products predicted by the 1D approximation are in good agreement with the multi-dimensional simulations. Further results were obtained exclusively with the 1D model.

The single phase turbulent boundary layer flow was modeled using the $k-\omega$ long time averaged turbulence model and incorporates exothermic tar decomposition reactions. This model is well suited for the present flat-plate reactor due to its ability to treat wall roughness and wall blowing (due to pyrolysis products ejected from the particles) in a relatively simple manner through boundary conditions. The individual particle trajectories were

then modeled based on a prolate spheroid particle drag coefficient and on contact friction with the wall. Extensive studies of these equations showed that the individual particle pyrolysis evolution is effectively de-coupled from temporal disturbances of the temperature and pressure boundary conditions on the flow side of the particle. This means that the particle responds to only time averaged values of the flow properties, and greatly simplifies the solution procedure.

The final forms of the equations were then coupled in order to simulate the entire steady-state flat-plate pyrolysis reactor. The efficiency factor for the reactor was defined as the ratio of the mass of tar exiting the reactor to the mass inflow rate of raw biomass feedstock. Examinations of this ratio calculated from a variety of simulations were then used to study the effects of particle size, wall temperature and mass feed rate. It was found that the efficiency can surpass fifty percent and improves with decreasing particle size. A more complex behavior was observed for the effects of reactor temperature which showed an optimal value for wall temperatures of approximately $800K$. Finally, only negligible effects of mass feed rate effects were observed within the range of parameters of the model assumptions. This was found to be a consequence of the fact that nearly all of pyrolysis occurs on the wall side of the particle, effectively de-coupling the pyrolysis from the gas flow such that it is predominantly a function of the wall temperature for any given particle size. These results explain why direct-contact reactors have the potential for marked increases in pyrolyzing efficiency as compared to non-contact and partial contact reactors.

ACKNOWLEDGMENTS

This research was conducted at the Jet Propulsion Laboratory (JPL) and sponsored by the U.S. Department of Energy (DOE), with Mr. Neil Rossmcissl (DOE Headquarters) and Mr. D. Hooker (DOE Golden Center) serving as contract monitors, under an agreement with the National Aeronautics and Space Administration. Computational resources are provided by the super computing facility at JPL.

REFERENCES

- D. Anderson, J. Tannehill, and R. Pletcher. *Computational Fluid Mechanics and Heat Transfer*. Hemisphere Publishing Corp., New York, New York, 1984.
- L. Burmeister. *Convective Heat Transfer*. John Wiley and Sons, New York, New York, 1983.
- E. (lot-net, D. Wang, D. Montanc, and S. Czernik. Hydrogen production by fast pyrolysis of biomass and catalytic steam reforming of pyrolysis oil. In A. V. Bridgwater, editor, *Advances in Thermochemical Biomass Conversion, volume 1*, pages 246-262. Blackie Academic and Professional, New York, New York, 1994.
- R. Clift, J. Grace, and M. Weber. *Bubbles, Drops and Particles*. Academic Press, New York, New York, 1978.
- L. J. Curtis and D. J. Miller. Transport model with radiative heat transfer for rapid cellulose pyrolysis. *Ind. Eng. Chem. Res.*, 27:1775-1783, 1988,
- (. Di Blasi. Analysis of convection and secondary reaction effects within porous solid fuels undergoing pyrolysis. *Combust. Sci. and Tech.*, 90:315-340, 1993.
- J. P. Diebold and A. Power. Engineering aspects of the vortex pyrolysis reactor to produce primary pyrolysis oil vapors for use in resins and adhesives. in A. V. Bridgwater and J. L. Kuester, editors, *Research in Thermochemical Biomass Conversion*, pages 609-628, Elsevier Applied Science, New York, New York, 1988.
- R. Graham, B. Frecl, D. Huffman, and M. Bergougnou. Applications of rapid thermal processing of biomass. In A. V. Bridgwater, editor, *Advances in Thermochemical Biomass Conversion*, volume 2, pages 1275--1288. Blackie Academic and Professional, New York, New York, 1994.
- M. Iussainov, A. Kartushinsky, A. Mulgi, U. Rudi, and S. Tisler. Experimental and theoretical study of the distribution of mass concentration of solid particles in the two-phase laminar boundary layer on a flat plate. *Int. J. Multiphase Flow*, 21(6):1141-1161, 1995.

C. A. Koufopoulos, N. Papayannakos, G. Maschio, and A. Lucchesi. Modelling of the pyrolysis of biomass particles. studies on kinetics, thermal and heat transfer effects. *Can. J. Chem. Eng.*, 69:907-915, 1991.

K. S. Lim, J. X. Zhu, and J. R. Grace. Hydrodynamics of gas-solid fluidization. *Fuel*, 21(Suppl.): 141-193, 1995.

R. S. Miller and J. Bellan. Analysis of reaction products and conversion time in the pyrolysis of cellulose and wood particles. *Comb. Sci. Tech.*, 1996a, in Press.

R. S. Miller and J. Bellan. A generalized biomass pyrolysis model based on superimposed cellulose, hemicellulose and lignin kinetics. *Comb. Sci. Tech.*, 1996b. Submitted.

R. S. Miller and J. Bellan. Tar yield and collection from the pyrolysis of large biomass particles. *Comb. Sci. Tech.*, 1996c. Submitted.

D. L. Pyle and C. A. Zaror. Heat transfer and kinetics in the low temperature pyrolysis of solids. *Chem. Eng. Sci.*, 39(1):147-158, 1984.

D. S. Scott and J. Piskorz. The flash pyrolysis of aspen-poplar wood. *Can. J. Chem. Eng.*, 60:666-674, 1982.

D. S. Scott, J. Piskorz, M. A. Bergougnou, R. Graham, and R. P. Overend. The role of temperature in the fast pyrolysis of cellulose and wood. *Ind. Eng. Chem. Res.*, 27:8-15, 1988.

SERI. A survey of biomass gasification: Volume II - Principles of gasification. Technical Report TR-33-239, Solar Energy Research Institute, Golden, Colorado, July 1979.

J. Szekeley and R. Carr. Heat transfer in a cyclone. *Chem. Eng. Science*, 21:1119-1132, 1966.

B. M. Wagenaar, J. A. M. Kuipers, W. Prim, and W. P. M. van Swaaij. The rotating cone flash pyrolysis reactor. in A. V. Bridgwater, editor, *Advances in Thermochemical Biomass Conversion*, volume 2, pages 1122-1133. Blackie Academic and Professional, New York, New York, 1994.

D. Wilcox. Reassessment of the scale-determining equation for advanced turbulence models. *AIAA Journal*, 26(11):1299-1310, 1988.

D. Wilcox. *Turbulence Modeling for CFD*. Griffin Printing, Glendale, California, 1993.

TABLES

Property	Value	Source
ρ_0	$650 \frac{kg}{m^3}$	Koufopoulos <i>et.al.</i> (1991)
ε_0	0.7	SERI (1979)
$\hat{\rho}$	$2167 \frac{kg}{m^3}$	
C	$2.3 \frac{kJ}{kg \cdot K}$	Curtis & Miller (1988)
λ	$1.256 \times 10^{-4} \frac{kJ}{m \cdot s \cdot K}$	Pyle & Zaror (1984)
Γ	0.05 <i>Darcys</i>	SERI (1979)

Table 1: Property values for wood. The conductivity and permeability values correspond to the cross grain direction(x_2) for 2D simulations.

FIGURE CAPTIONS

Figure 1: Schematic of the idealized flat-plate boundary layer reactor depicting three individual particles and their corresponding velocities (not to scale).

Figure 2: Velocity vectors for a 2D wood particle with aspect ratio $\Theta = 2$ ($x_1 = 0$ is a plane of symmetry) at a time corresponding to 40% reduction of the virgin wood mass; (a) $l'_{11}/l'_{22} = 1$, (b) $l'_{11}/l'_{22} = 10$, (c) $l'_{11}/l'_{22} = 100$. The particle height is $l_2 = 5mm$, and the heating conditions are $T'_w = T'_\infty = 900K$.

Figure 3: Comparison of 1D and 2D particle pyrolysis simulation tar collections for various ratios of the parallel to cross grain permeability. The particle height is $l_2 = 5mm$, with $\Theta = 2$, and the heating conditions are $T'_w = T'_\infty = 900K$.

Figure 4: Comparison of 1D and 2D particle pyrolysis simulation tar collections for various particle aspect ratios, The particle height is $l_2 = 5mm$, and the heating conditions are; $T'_w = T'_\infty = 900K$.

Figure 5: Comparison of 1D and 2D particle pyrolysis simulation tar collections for various ratios of the parallel to cross grain thermal conductivity, The particle height is $l_2 = 5mm$, with $\Theta = 2$, and the heating conditions are $T'_w = T'_\infty = 900K$.

Figure 6: Comparison of (a) tar collections and (b) mass averaged particle temperature obtained through exclusive heating at either the wall or the flow boundary for 1D particle pyrolysis employing the complete momentum equation [15] with $l_2 = 5mm$ and $T'_w, T^* = 900K$.

Figure 7: Illustration of the turbulent flat-plate boundary layer simulation; (a) numerical grid, (b) steady-state temperature contours. inflow conditions are $u_{inflow} = 50m/s, T'_{inflow} = 400K$, and the wall is at $T'_w = 900K$.

Figure 8: Temporal history of pressure and temperature extracted from the steady-state boundary layer flow field at position $x_2 = 1.5mm$ and obtained from a solution of the particle trajectory equations [31]-[35] for a particle with $l_2 = 1mm$. Both t_c and $m_p(t)$ were obtained from a 1D particle simulation assuming constant $T^* = 850K$ and $p^* = 150kPa$.

Figure 9: Temporal evolution of the tar collection for a 1D particle simulation having $T^* = 850 + 50 \sin(\omega't)$. The simulation conditions are $l_2 = 1 \text{ mm}$ and $T_w = 900K$.

Figure 10: Temporal development of apparent char density profiles during a 1D particle simulation. The simulation conditions are $l_2 = 1 \text{ rent}$, $T_w = 900K$, $T^* = 850K$ and the profiles correspond to times; $t/t_c = 0.25, 0.5, 0.75, 1.0$.

Figure 11: Steady state tar mass fraction from a fully coupled flat-plate reactor simulation having flow conditions: $u_{\text{inflow}} = 50m/s$, $T_{\text{inflow}} = 400K$, $T_w = 900K$, particle conditions; $l_2 = 2.5mm$, $\Theta = 2$, and $\dot{m}_{\text{feed}} = 10kg/hr$: (a) tar boundary layer contours, (b) tar fraction profiles at various x_1 locations,

Figure 12: Reactor efficiency factor as a function of the particle feed size. The reactor conditions are: $u_{\text{inflow}} = 50m/s$, $T_{\text{inflow}} = 400K$, $T_w = 900K$, $\Theta = 2$, and $\dot{m}_{\text{feed}} = 10kg/hr$.

Figure 13: Reactor efficiency factor as a function of the wall temperature for various particle sizes. The reactor conditions are: $u_{\text{inflow}} = 50m/s$, $T_{\text{inflow}} = 400K$, $\Theta = 2$, and $\dot{m}_{\text{feed}} = 10kg/hr$. The kinetic limit is obtained by neglecting tar decomposition reactions.

Figure 14: Reactor efficiency factor as a function of the feedstock mass injection rate. The reactor conditions are: $u_{\text{inflow}} = 50771/s$, $T_{\text{inflow}} = 400K$, $T_w = 900K$, $l_2 = 2.5mm$, and $\Theta = 2$.

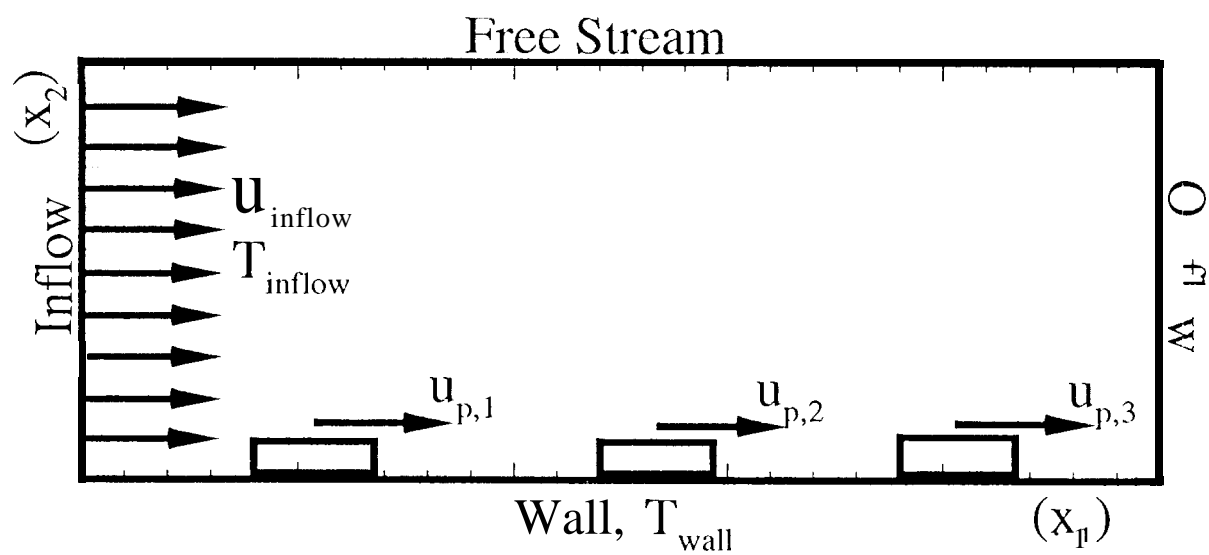


Figure 1

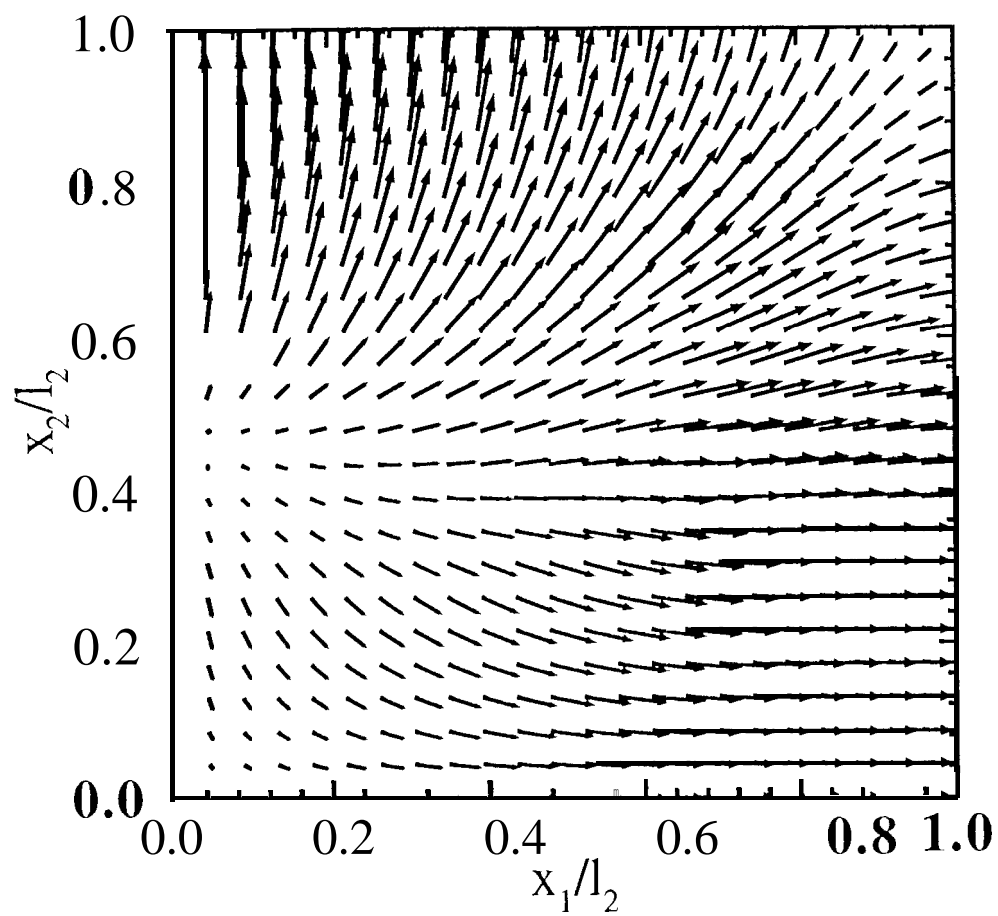


Figure 2a

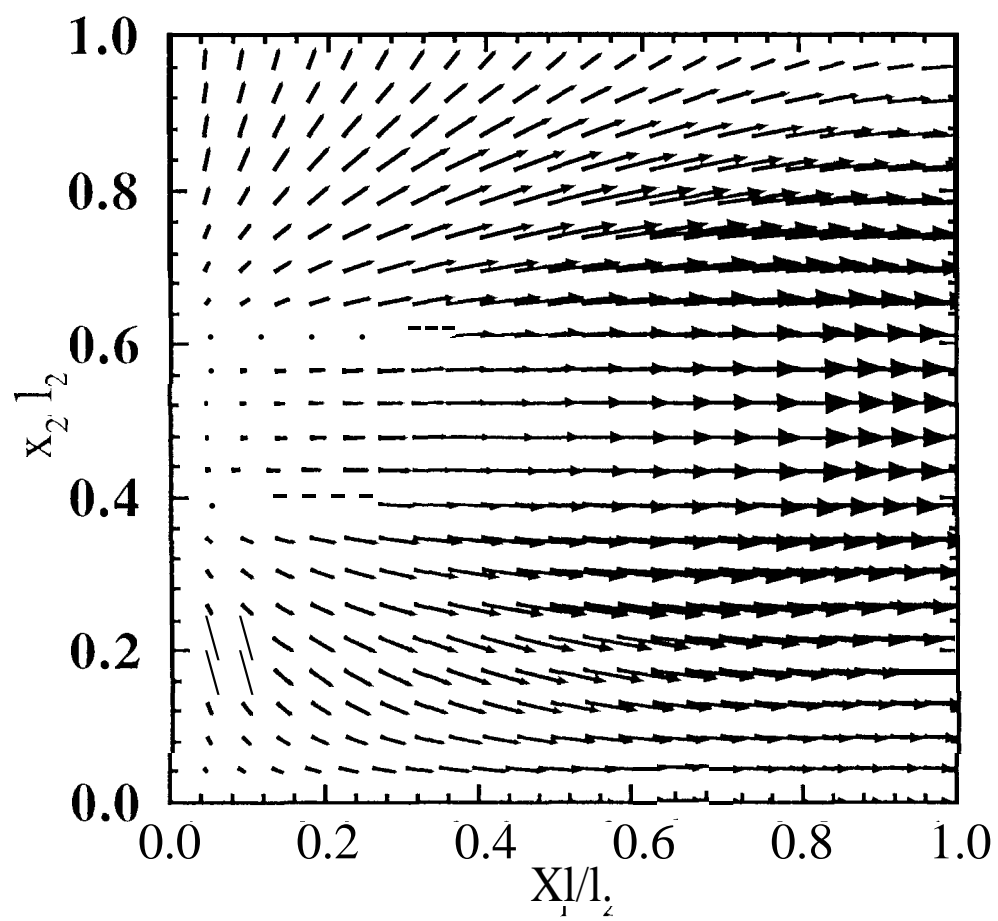


Figure 2b

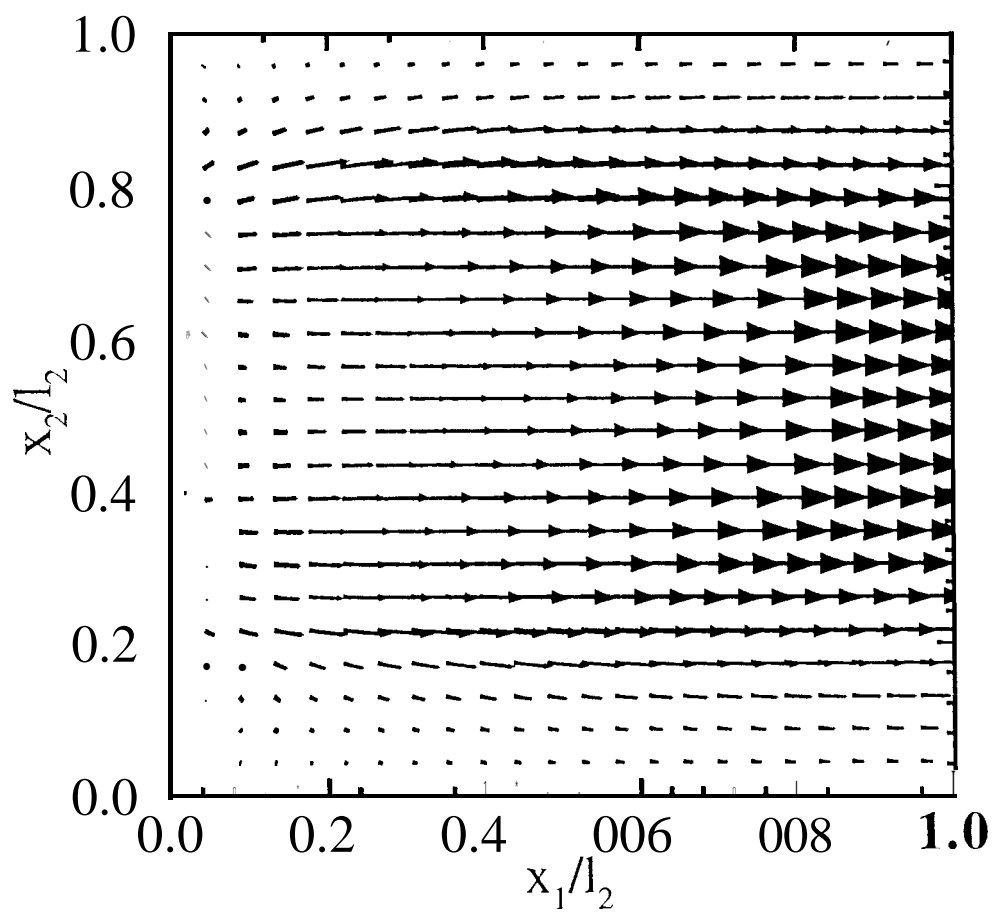


Figure 2c

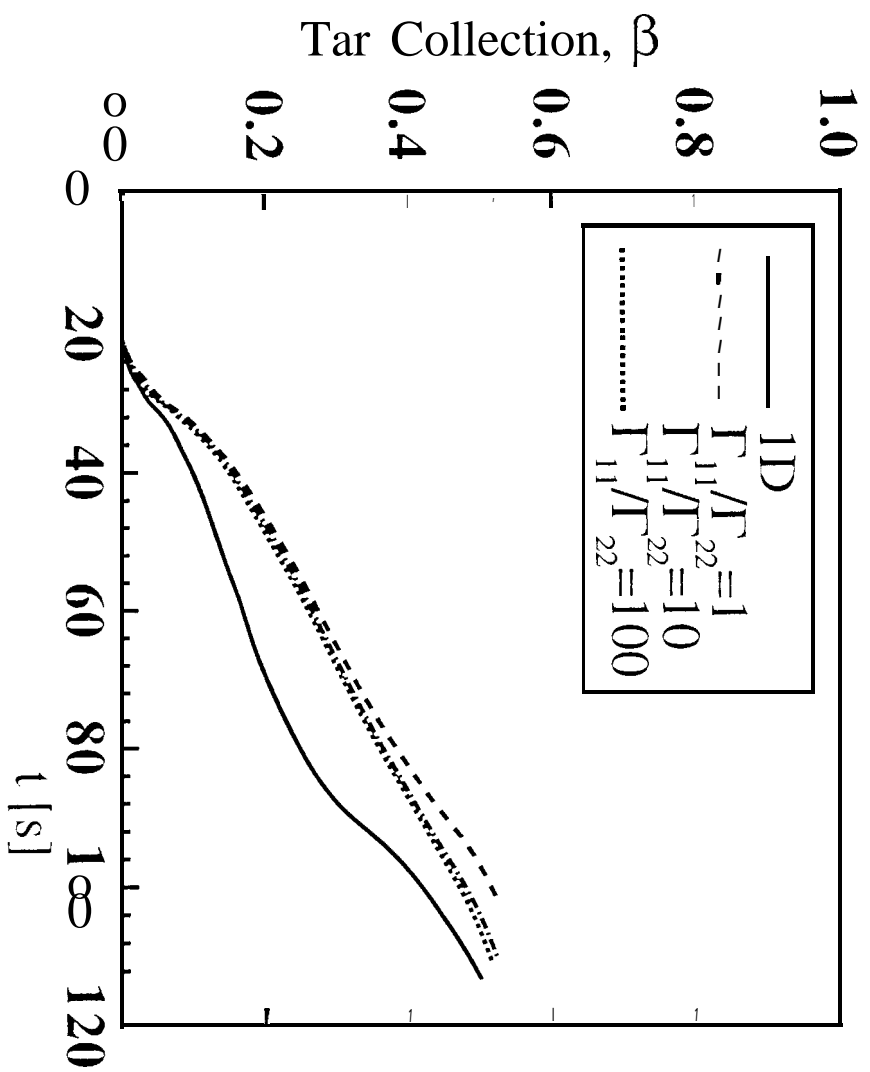


Figure 3

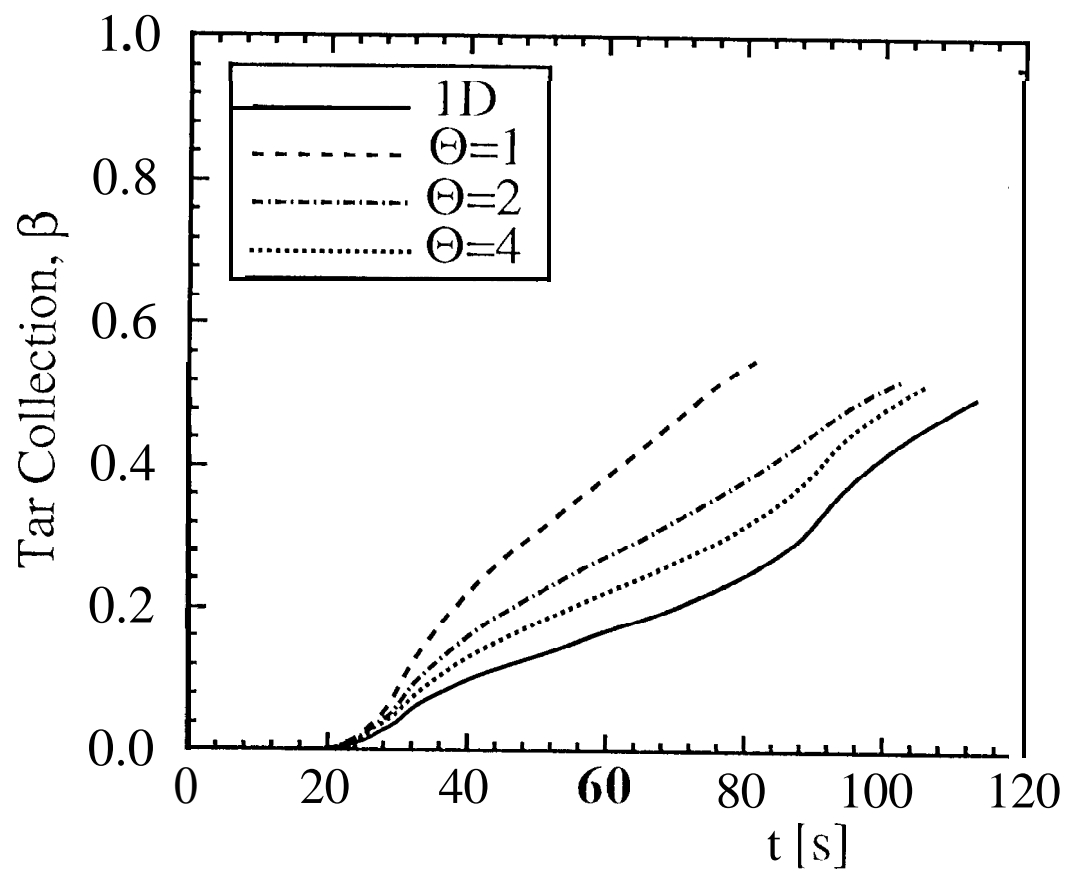


Figure 4

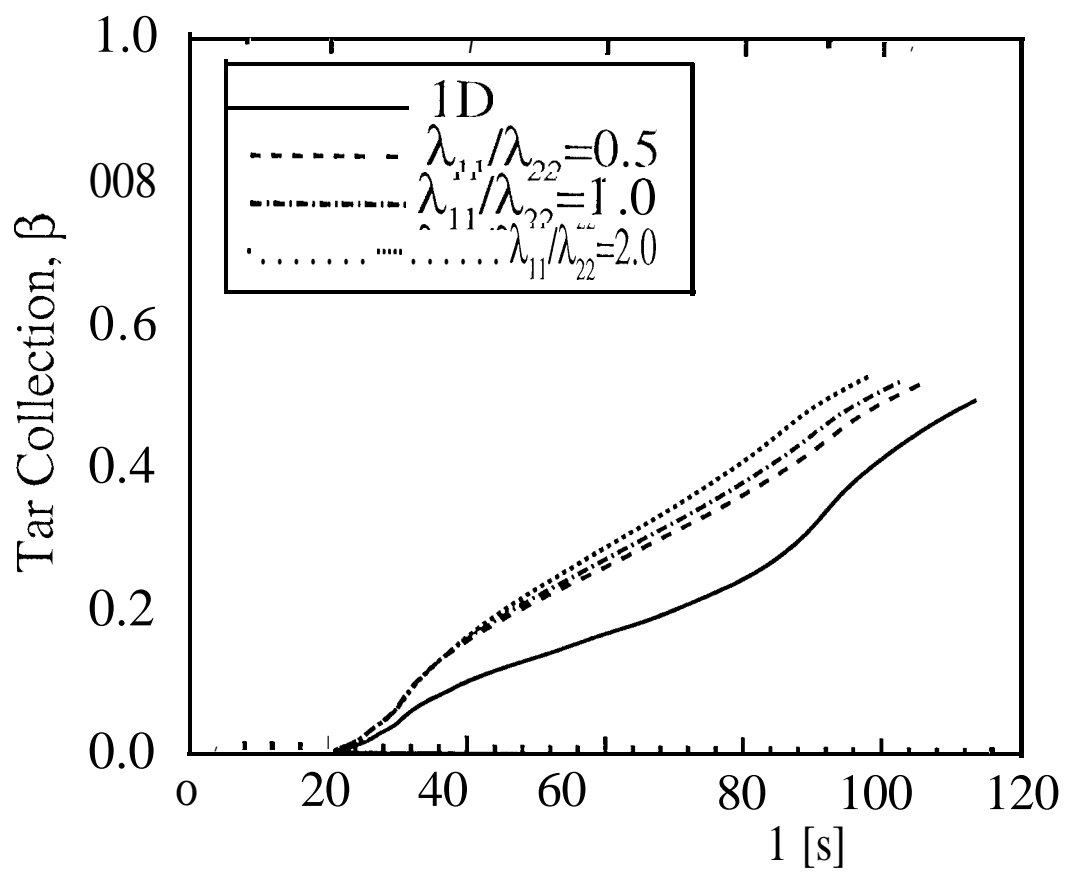


Figure 5

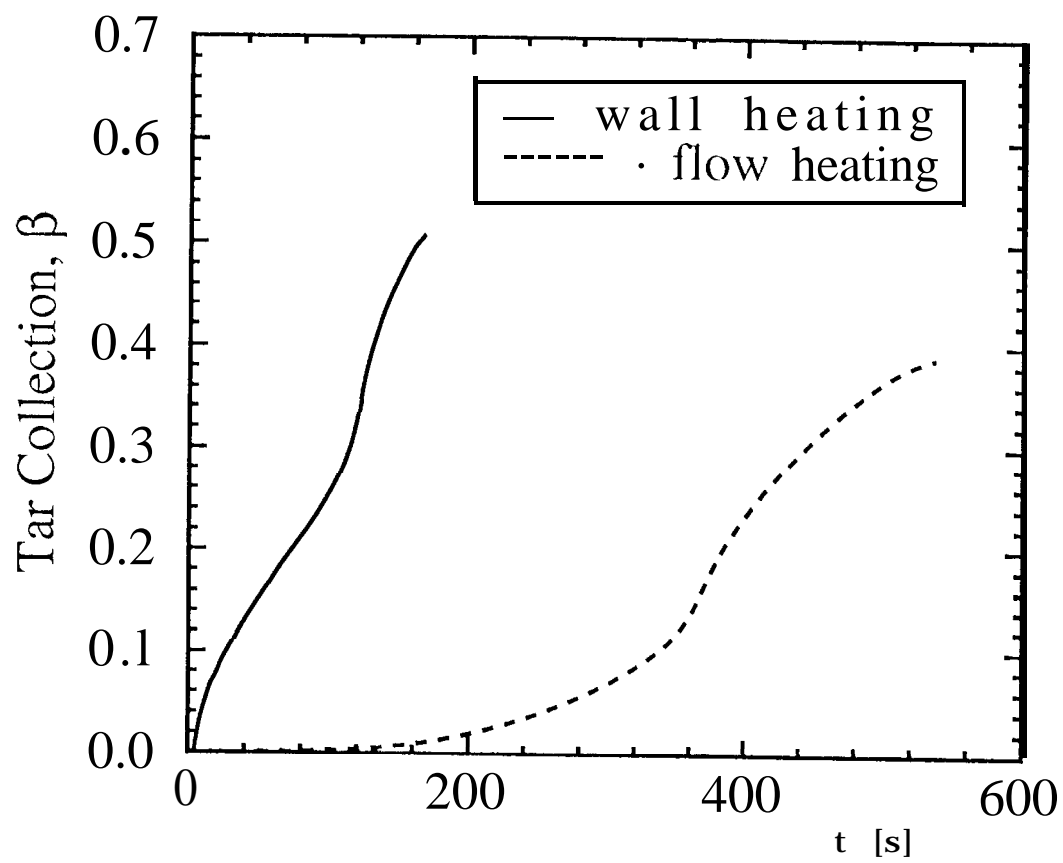


Figure 6a

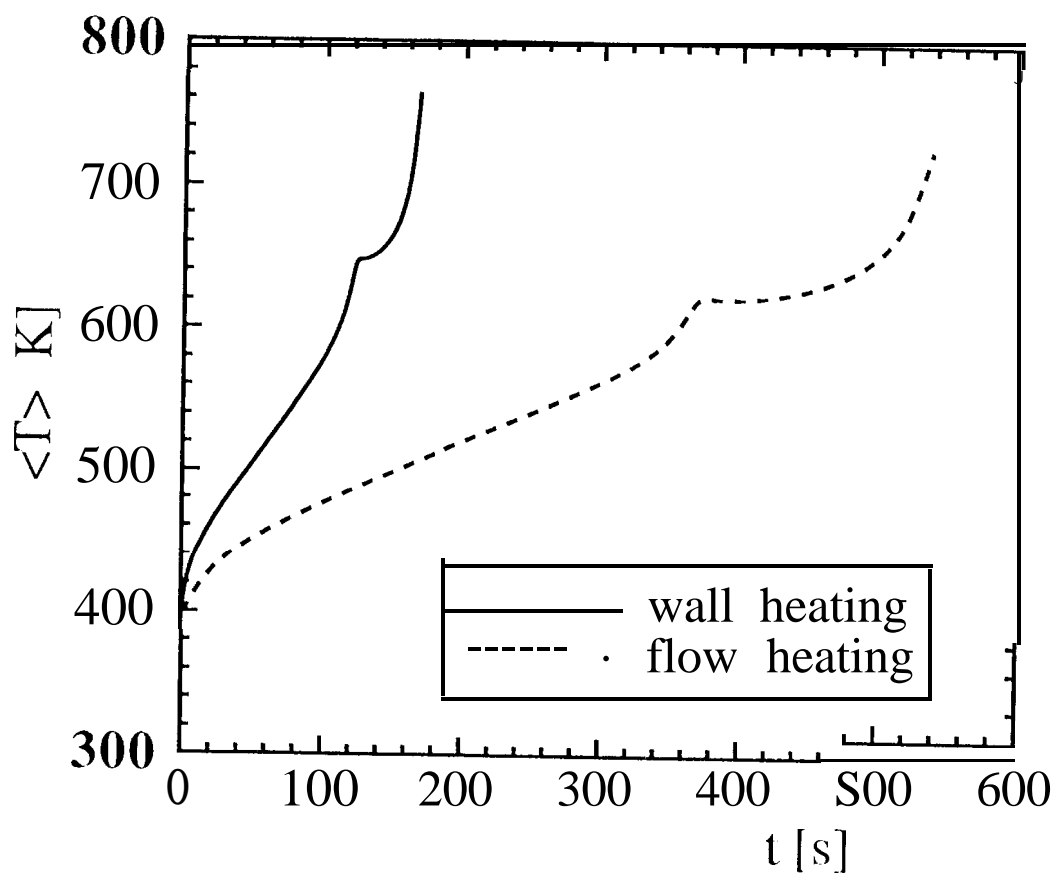


Figure 6b

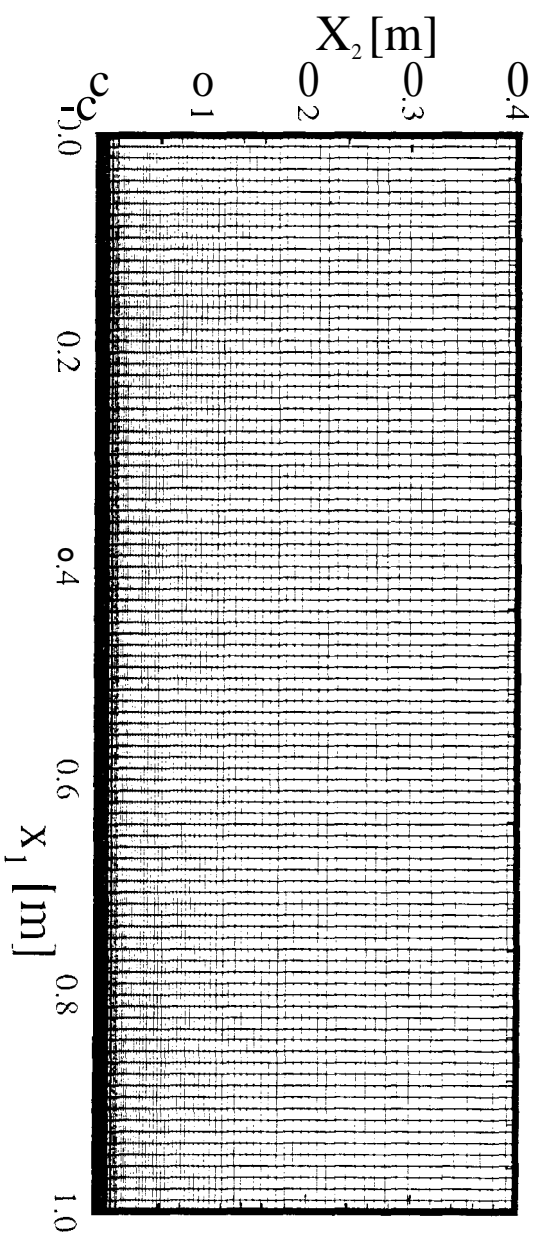


Figure 7a

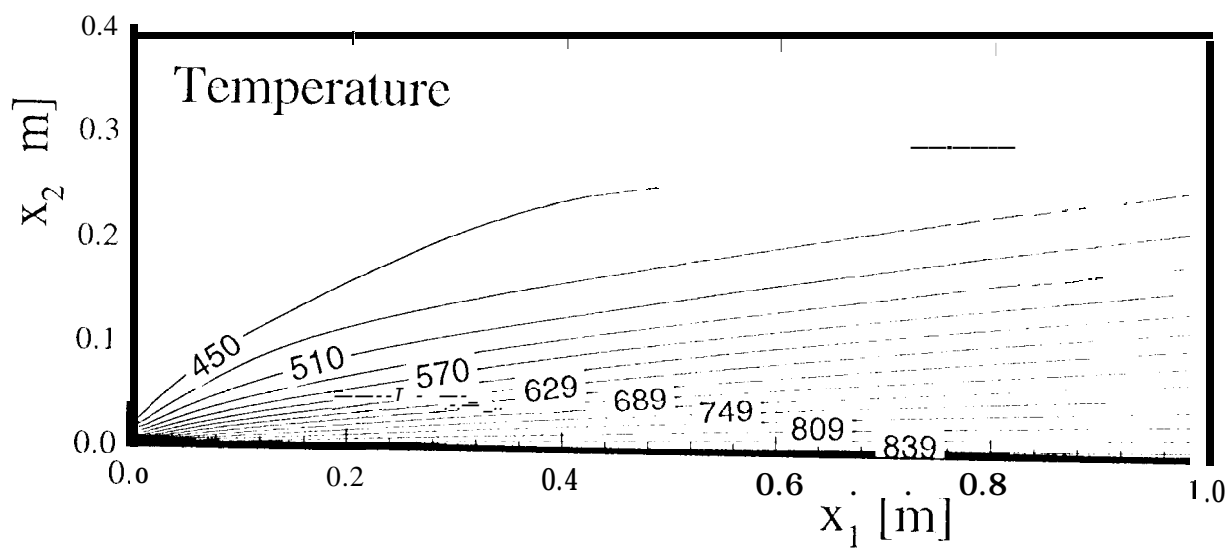


Figure 7b

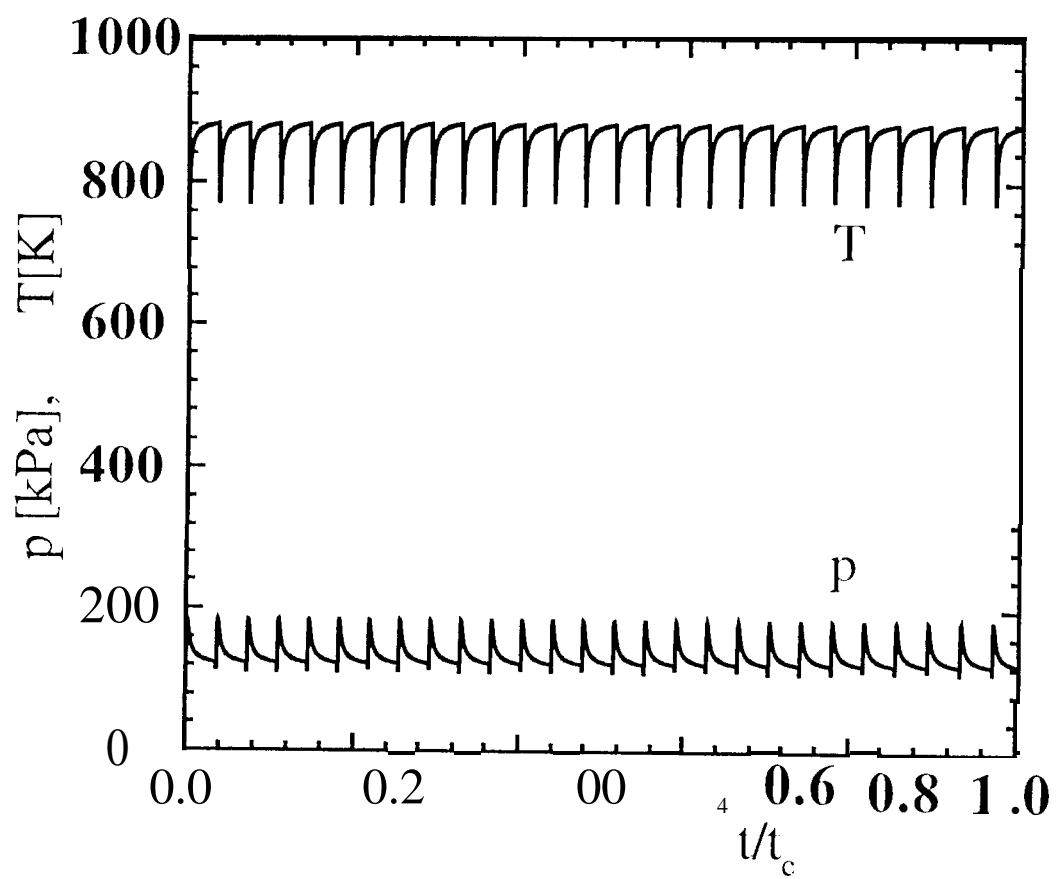


Figure 8

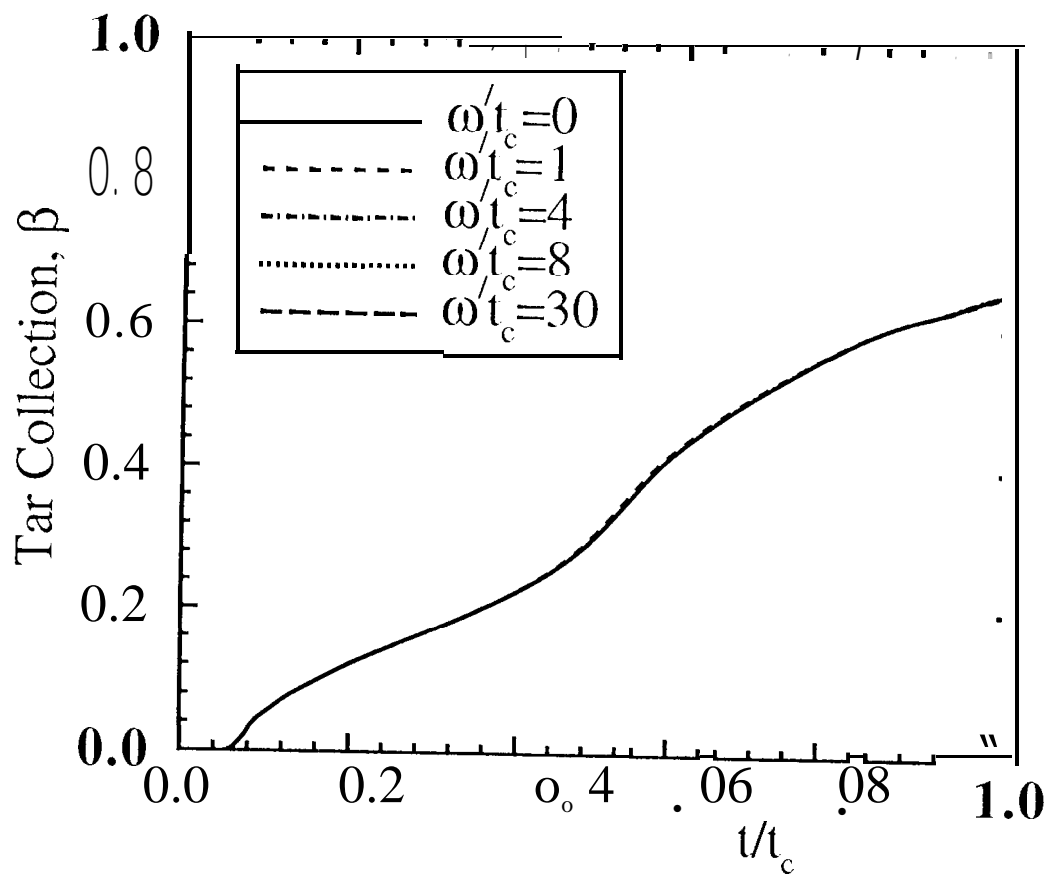


Figure 9

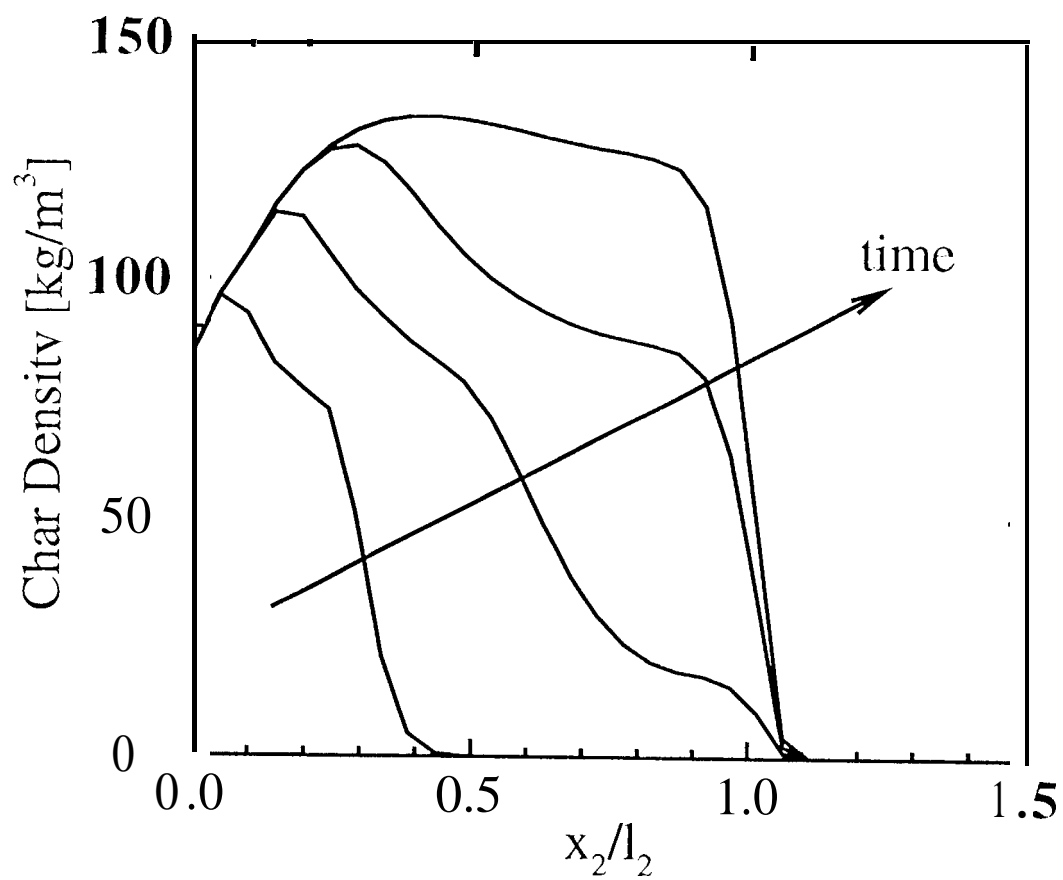


Figure 10

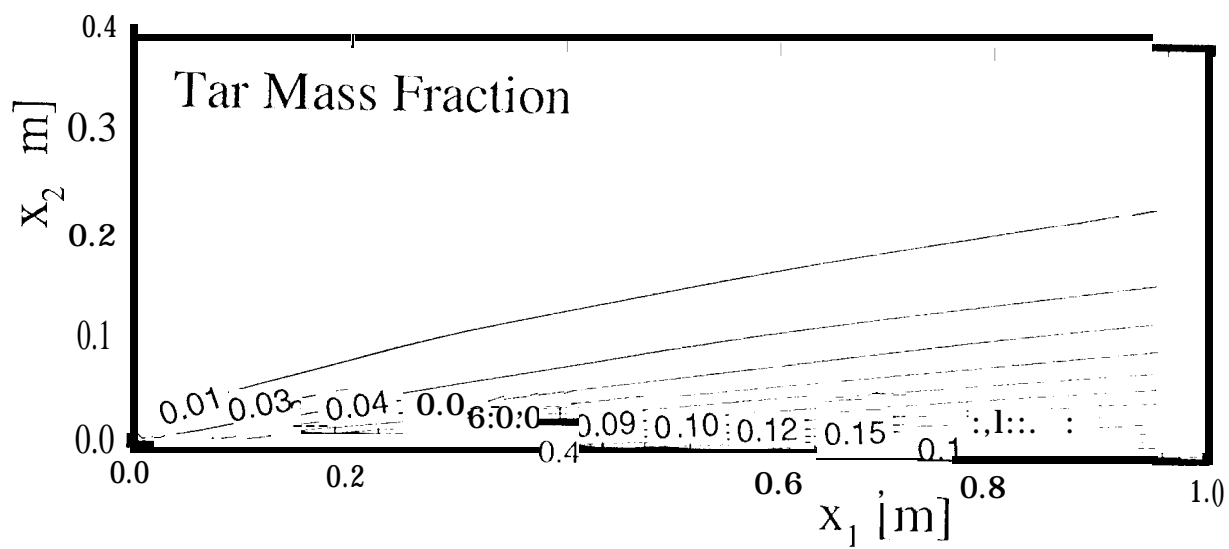


Figure 11a

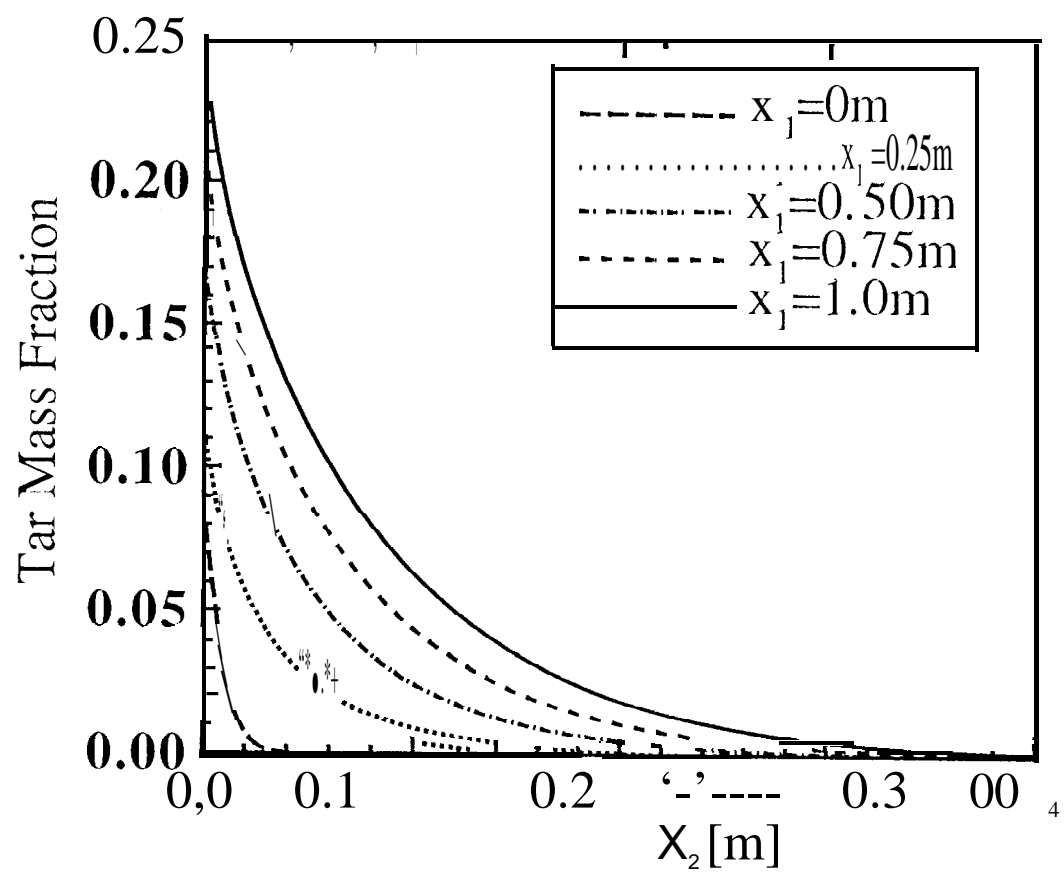


Figure 11b

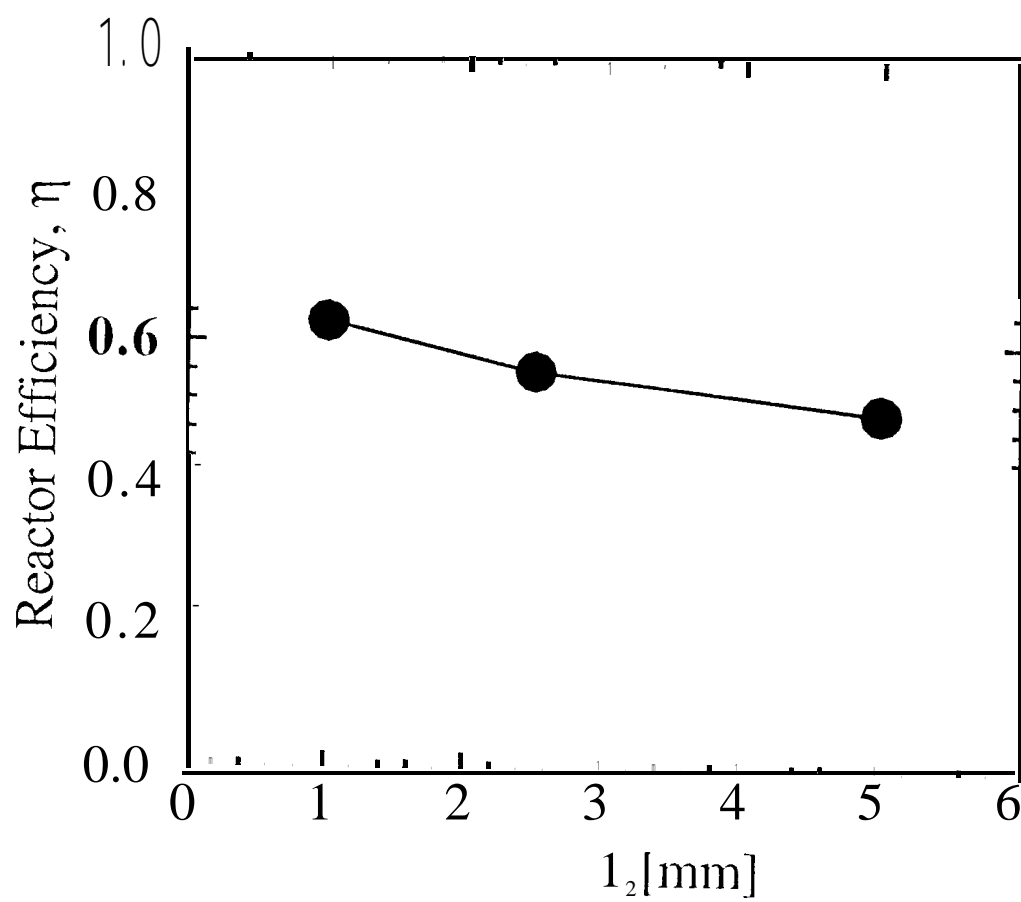


Figure 12

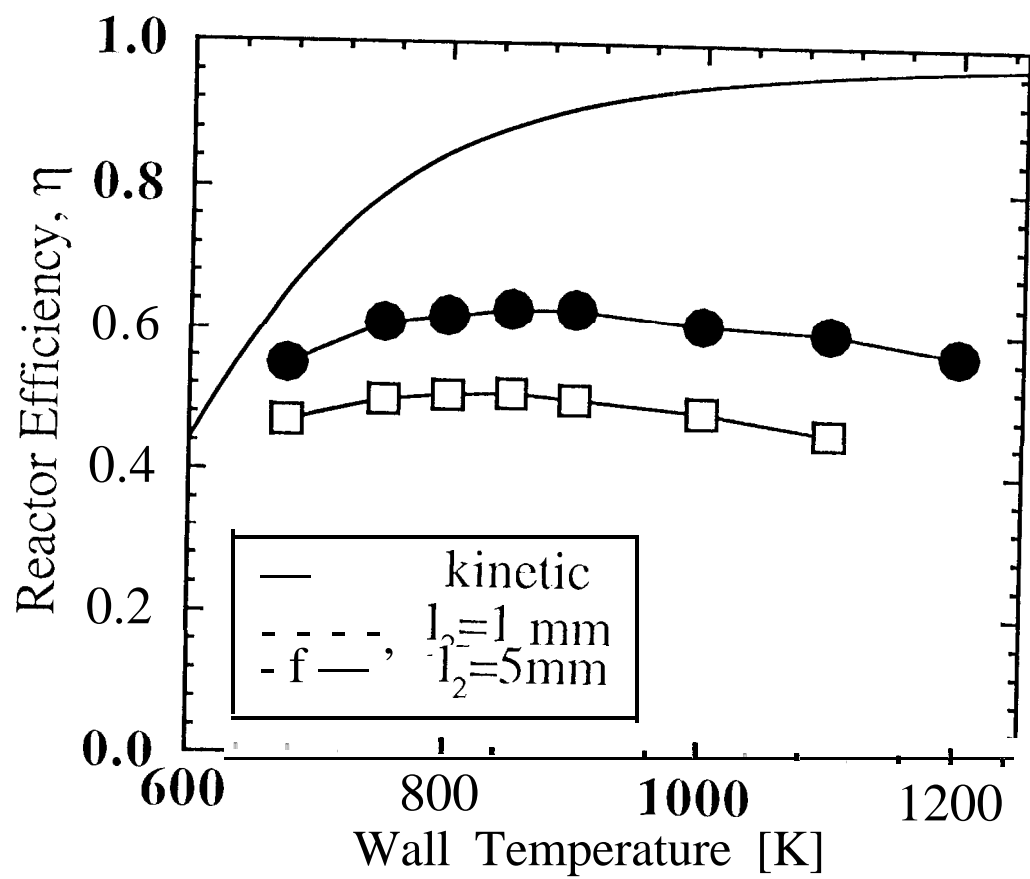


Figure 13

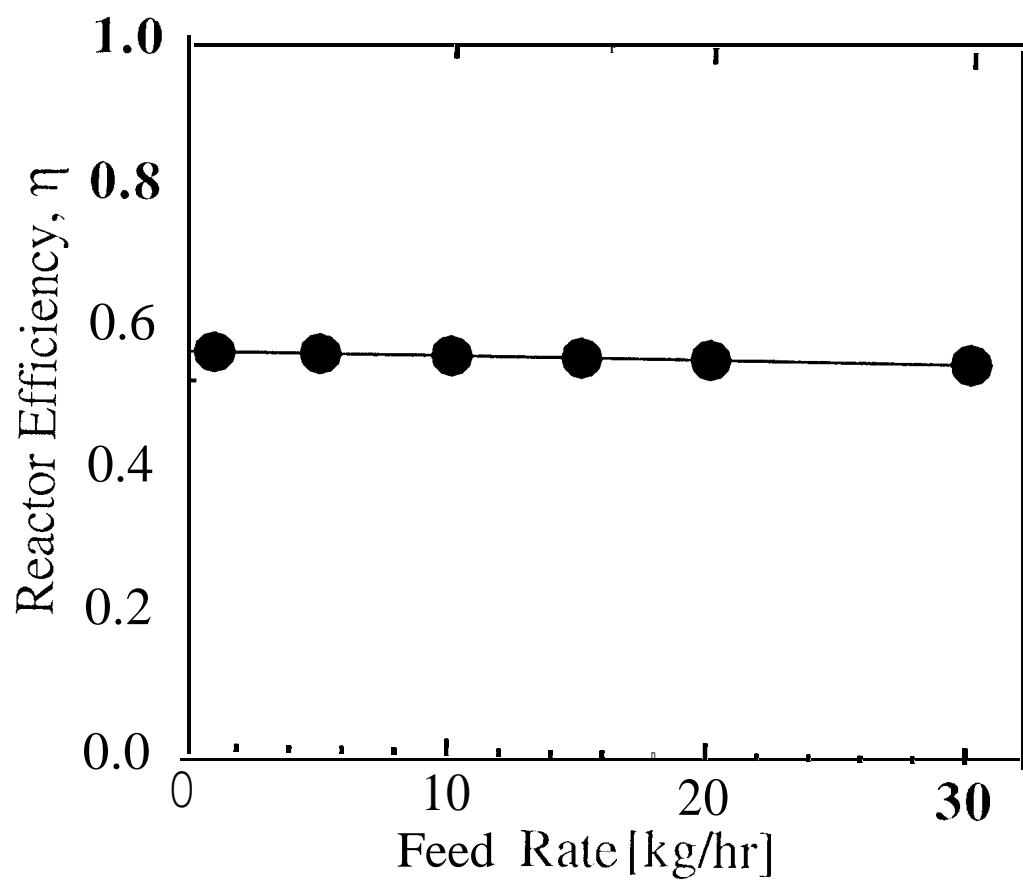


Figure 14